Osseointegration Assessment of 3D-printed Porous Structure with Bone-mimetic Irregular Design

Hun Yeong Ban

The Graduate School
Yonsei University
Graduate Program of Biomedical Engineering

Osseointegration Assessment of 3D-printed Porous Structure with Bone-mimetic Irregular Design

A Dissertation Submitted
to the Graduate Program of Biomedical Engineering
and the Graduate School of Yonsei University
in partial fulfillment of the
requirements for the degree of
Doctor of Philosophy

Hun Yeong Ban

December 2024

This certifies that the Dissertation
of Hun Yeong Ban is approved

Thesis Supervisor Jong-Chul Park

Thesis Committee Member Min-gu Kim

Thesis Committee Member Jayoung Kim

Thesis Committee Member Dohyung Lim

Thesis Committee Member Bomi Gweon

The Graduate School
Yonsei University
December 2024

TABLE OF CONTENTS

LIST OF FIGURES iii

LIST OF TABLES vii

ABSTRACT viii

I. BACKGROUNDS 1

1. Porous structure as an alternative to traditional bone cement 1

2. Emergence of 3D printing in porous structure production 3

3. Challenges: developing bone-mimetic designs 5

4. Challenges: optimizing 3D printing process parameters 8

II. OBJECTIVES AND SCOPES 11

III. MATERIALS AND METHODS 12

1. Porous structure modeling 12

1.1. Bone-templated porous structure 12

1.2. Regular lattice porous structure 13

1.3. Irregular porous structure 14

2. Specimen fabrication 17

3. Pore shape characterization 22

4. Mechanical testing 24

5. Animal implantation 25

5.1. Animal prepration·····25
5.2. Surgical procedure·····25
5.3. Postoperative care and sacrifice·····28
6. Histological analaysis·····29
6.1. Slide preparation and staining·····29
6.2. Bone histomorphometry·····29
7. Statistical analaysis·····31
IV. RESULTS AND DISCUSSION·····32
1. Minimization of pore shape error in SLM manufacturing·····32
2. Determination of mechanical properties by pore shape error·····41
3. Enhancement of osseointegration·····52
V. CONCLUSION·····57
APPENDIX·····60
REFERENCES·····63
ABSTRACT (IN KOREAN)·····74

LIST OF FIGURES

Figure 1. Comparative illustration of bone-to-implant fixations using (a) traditional bone cement and (b) a porous structure·····2

Figure 2. Manufacturing technologies for porous structures: (a) plasma spraying, (b) bead sintering (diffusion bonding), and (c) selective laser melting (3D printing)·····4

Figure 3. Design approaches for bone-mimetic porous structures: (a) using a bone template, (b) using a unit cell, and (c) employing Voronoi tessellation (the illustrations provided are from the literature [19, 23, 25])·····7

Figure 4. Schematic representation of the SLM process along with the laser parameters·····10

Figure 5. Modeling of irregular porous structure·····13

Figure 6. Designed pore size distribution of irregular porous structure·····14

Figure 7. Modeling of regular lattice porous structure·····15

Figure 8. Modeling of bone-templated porous structure·····16

Figure 9. As-built parametric study specimens·····20

Figure 10. As-built in-vivo test specimens·····21

Figure 11. Micro-CT scan of the specimen·····22

Figure 12. Pore size measurements in each observation view·····23

Figure 13. Surgical procedure for animal implantation·····27

Figure 14. The process of bone histomorphometry from previous study [63]·····30

Figure 15. Pore size distributions at various laser powers (160-80 W) at a constant scan speed of 950 mm/s·····35

Figure 16. Pore size distributions at various scan speeds (550 – 950 mm/s) at a constant laser power of 100W·····36

Figure 17. Pore size distributions at various scan speeds (550 – 950 mm/s) at a constant laser power of 80W·····37

Figure 18. (a) Shape errors observed from the side view for various parameter settings; (b) Visualization of changes in pore shape based on the 3D-reconstructed models·····38

Figure 19. (a) Shape errors observed from the top view for various parameter settings; (b) Visualization of changes in pore shape based on the 3D-reconstructed models·····39

Figure 20. A schematic depicting how each pore in an irregular porous structure can be susceptible to overhang-induced shape error during the SLM process·····40

Figure 21. Compressive strengths of the specimens produced under various parameter settings (information for actual bone is sourced from the literature [72-75]). The results are presented as mean ± standard deviation with asterisks denoting $P < 0.05$·····45

Figure 22. Elastic modulus of the specimens produced under various parameter settings (information for actual bone is sourced from the literature [72-75]). The results are presented as mean ± standard deviation with asterisks denoting $P < 0.05$·····46

Figure 23. Scatter plots displaying the mechanical properties in relation to (a-b) side-view shape error and (c-d) top-view shape error. The R^2 value represents the coefficient of determination·····47

Figure 24. Stress-strain curves according to (a) various laser powers at a constant scan speed of 950 mm/s, (b) various scan speeds at a constant laser power of 100 W, and (c) various scan speeds at a constant laser power of 80 W (information for actual bone is sourced from the literature [82])·····50

Figure 25. Energy absorption-strain curves according to (a) various laser powers at a constant scan speed of 950 mm/s, (b) various scan speeds at a constant laser power of 100 W, and (c) various scan speeds at a constant laser power of 80 W (information for actual bone is sourced from the literature [82])·····51

Figure 26. Bone histomorphometry results: bone-to-implant contact (BIC) and absent area according to different implantation periods and porous structure designs. Asterisks denotes P < 0.05·····54

Figure 27. Bone histomorphometry results: bone area according to different implantation periods and porous structure designs. Asterisks denotes P < 0.05·····55

Figure 28. Representative histological images according to different implantation periods and porous structure designs.Blue pixels indicate bone area·····56

Figure A1. Side-viewed pore shape changes observed by optical microscopy according to different parameter sets·····60

Figure A2. Top-viewed pore shape changes observed by optical microscopy according to different parameter sets·····61

Figure A3. (a) Densities of bulk solid specimens under different parameter sets; (b) Visualization of the internal defect changes using the 3D-reconstructed models·····62

LIST OF TABLES

Table 1. The chemical composition of the Ti-6Al-4V Grade 23 powder utilized in this study (expressed in weight percentage)·····17

Table 2. SLM process parameter settings used for parametric study specimens·····19

Table 3. SLM process parameter settings used for in-vivo test specimens·····21

Table 4. Changes of shape errors and mechanical properties in response to decreasing laser power (160-80 W) at a constant scan speed of 950 mm/s·····48

Table 5. Changes of shape errors and mechanical properties in response to increasing scan speed (550-950 mm/s) at a constant laser power of 100 W·····48

Table 6. Changes of shape errors and mechanical properties in response to increasing scan speed (550-950 mm/s) at a constant laser power of 80 W·····49

ABSTRACT

Osseointegration Assessment of 3D-printed Porous Structure with Bone-mimetic Irregular Design

Hun Yeong Ban

Graduate Program of Biomedical Engineering
The Graduate School, Yonsei University

The porous structure plays a critical role in inducing a stable biological anchorage between bone and implant, so-called osseointegration. It provides a vital alternative to traditional bone cement procedures. Meanwhile, 3D printing technologies have emerged as a robust manufacturing platform in orthopedics. In particular, selective laser melting (SLM) stands out in its excellent resolution. Naturally, it has become one of the current major trends to incorporate highly bone-mimetic porous structures into orthopedic products using SLM.

Recently, Voronoi tessellation has been identified as a promising modeling technique for designing a porous structure closest to the actual bone by implementing irregularly sized pores. However, several challenges remain in the

clinical application of the resulting porous structures. Firstly, there is a lack of verification regarding their biological performance. Secondly, there is a need for a better understanding of fine-tuning the manufacturing process to ensure the quality of such complex porous structures.Thus, this study aimed to propose available references addressing the existing concerns.

In detail, we developed an irregular porous structure using a customized algorithm based on Voronoi tessellation. Firstly, for optimizing the manufacturing process using SLM, we fabricated the specimens at different parameter settings. Specifically, the laser power and scan speed varied at 80-160 W and 550-950 mm/s, respectively. Afterward, the pore shape error was manually measured using micro-CT images, and the mechanical properties were obtained through compression tests. As a result, the pore narrowed in response to stronger laser powers and slower scan speeds, more dominantly altered by the former. In addition, greater dimensional inaccuracies led to higher mechanical properties, showing a positive correlation. Consequently, the combination of the weakest laser power (80 W) and the fastest scan speed (950 mm/s) exhibited the closest pore size distribution to the design with minimized shape errors of 135-150 μm while maintaining clinically acceptable levels of compressive strength and elastic modulus (131.45 MPa and 6.24 GPa, respectively).

Then, we examined its osseointegration capacity with conventional ones, including a bone-templated porous structure and a regular lattice porous structure. This comparative analysis involved fabricating specimens using an SLM machine and Ti-6Al-4V powder and implanting them into animals for bone histomorphometry. As a result, the irregular porous structure exhibited comparable

in-vivo outcomes to the bone-templated porous structure, showing a significant improvement over the regular lattice porous structure in retaining bone formation during the mid-term implantation period.

Collectively, our efforts here have underlined the following points: 1) The importance of adopting the actual bone irregularity in designing a porous structure to enhance osseointegration. 2) The necessity of establishing separate parameter settings for such complex porous structures in the SLM process, focusing on minimizing shape error. These findings may provide valuable insights for designing and manufacturing the latest orthopedic implants, including porous components (or areas).

Keywords: Irregular Porous Structure · Osseointegration · 3D Printing · Selective Laser Melting · Parametric Study · Shape Error · Mechanical properties

I. BACKGROUNDS

1. Porous structure as an alternative to traditional bone cement

In orthopedic surgeries, the success of clinical outcomes heavily depends on the fixation between implants and bone [1]. Traditionally, bone cement has been widely used for this fixation. However, some follow-up studies indicate a substantial risk of aseptic loosening, requiring revision surgery. This issue arises when debris generated from the bone cement due to inadequate fixation and subsequent micro-motion leads to osteolysis [2, 3].

Therefore, incorporating porous structures into orthopedic implants has been favored as an alternative strategy to traditional bone cement procedures, providing improved results for aseptic loosening [4, 5]. The prevailing belief is that the porous structure creates a strong biological fixation by encouraging cell ingrowth into the pores, ultimately facilitating osseointegration [6].

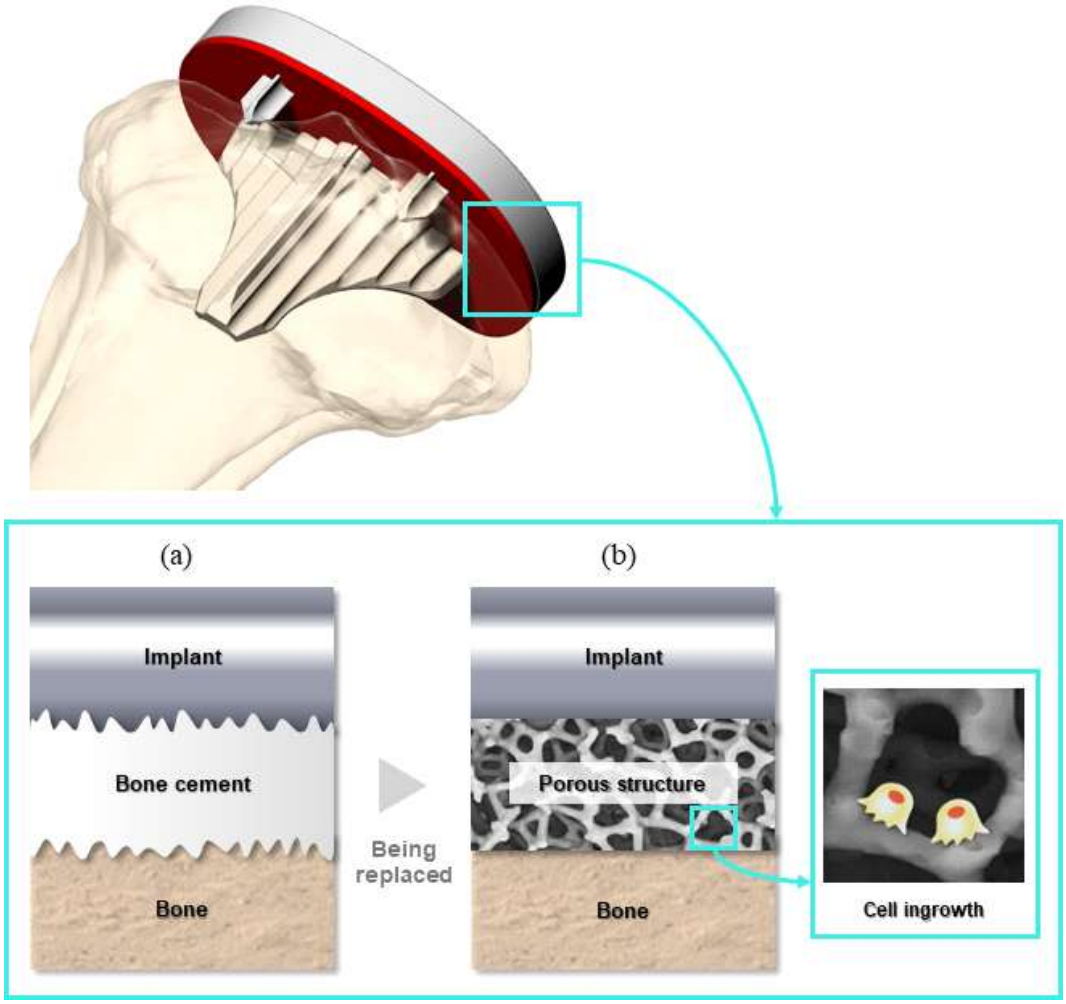

Figure 1. Comparative illustration of bone-to-implant fixations using (a) traditional bone cement and (b) a porous structure.

2. Emergence of 3D printing in porous structure production

Several coating methods, including plasma spraying and bead sintering (diffusion bonding), have previously been employed to create porous structures [7]. However, these technologies struggle with poor manufacturing resolutions, resulting in suboptimal pore sizes and porosities [8]. Furthermore, they face significant problems related to the delamination of the coated porous layers [9, 10].

Recently, 3D printing technologies have become a powerful manufacturing method for orthopedic implants. The 3D-printed porous structures can replace the conventionally coated ones with better pore shape resolution and resistance to peeling off [11]. In particular, among 3D printing technologies, selective laser melting (SLM) provides superior accuracy and precision compared to the others, including direct energy deposition (DED) and electron beam melting (EBM), even though it typically requires longer processing times [12, 13]. Consequently, using SLM to produce complex porous structures is becoming a significant trend in orthopedics [14, 15].

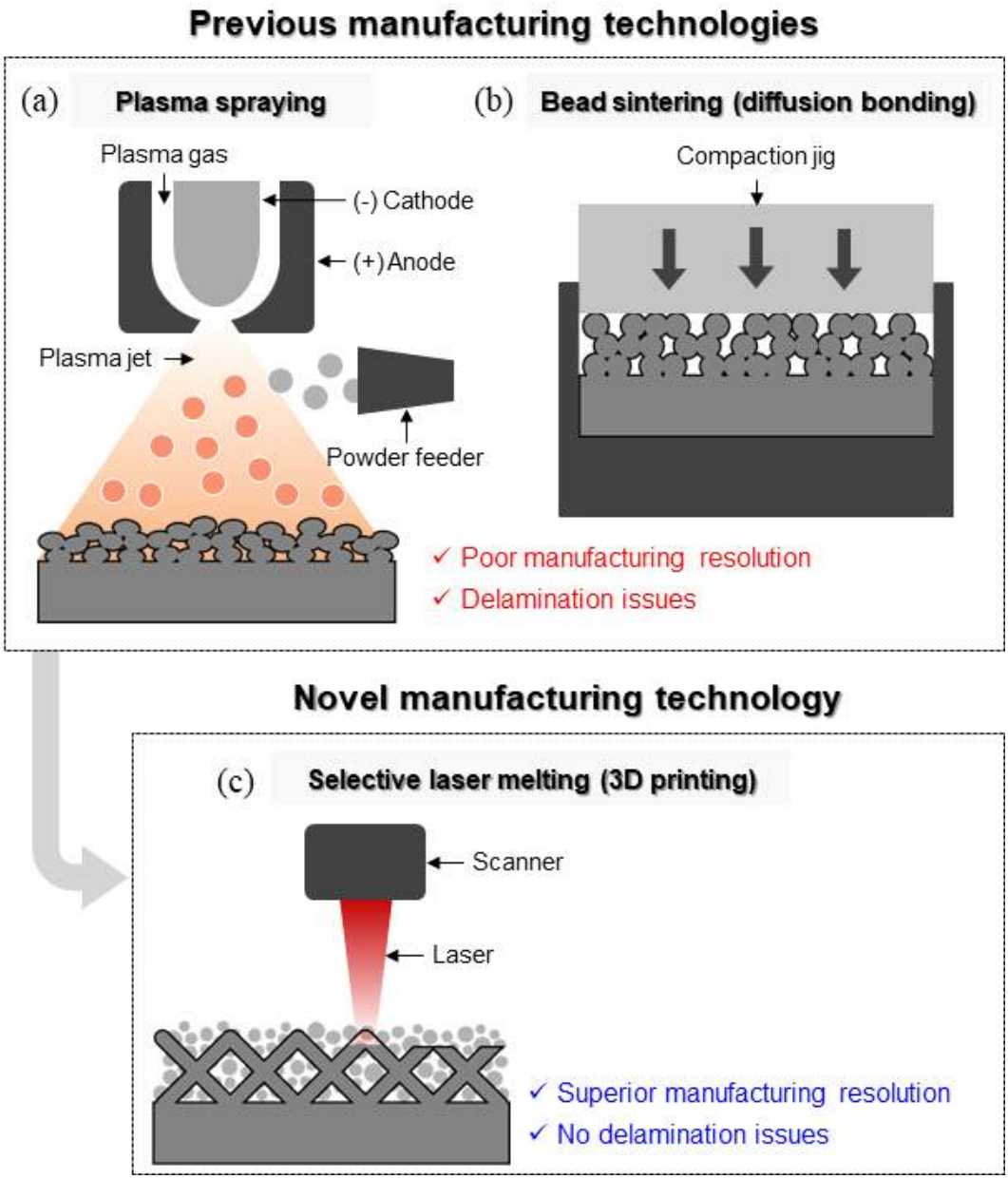

Figure 2. Manufacturing technologies for porous structures: (a) plasma spraying, (b) bead sintering (diffusion bonding), and (c) selective laser melting (3D printing).

3. Challenges: developing bone-mimetic designs

Recent advances in manufacturing, including the introduction of 3D printing technologies, have led to great interest in designing highly sophisticated porous structures that mimic cancellous bone and enhance osteointegration potential [16, 17].

Talukdar et al., Cheng et al. and Podshivalov et al. developed replicas of cancellous bone through micro-CT scanning and 3D reconstruction [18-20]. Specifically, the former two groups achieved excellent in-vitro and in-vivo results with their manufactured porous structures. However, while using an actual bone structure as a template is appealing in bio-inspired modeling, it has apparent drawbacks when applied to large-sized implants due to the limited volume available for acquisition. Therefore, many researchers have created porous structures using unit cells [21-23], which can continuously and infinitely expand. Nevertheless, human cancellous bone consists of interconnected pores of various diameters [24]. Thus, merely repeating unit cells—essentially fixing the pore size as a constant—may restrict potential factors that boost osteointegration.

There is growing attention to employing Voronoi tessellation as a prominent solution over the previous approaches mentioned above. This mathematical modeling technique allows for randomly generating numerous pores within a freely selected area, resulting in irregular pore sizes rather than a single fixed value. [25-27]. However, despite the opportunities to discover a significant enhancement in osseointegration, the related studies have mainly focused on design optimization. For example, Gómez extracted pore seeds of cancellous bone from the micro-CT

images and utilized this information to yield better bone replication [28]. Other studies have suggested functionally graded porosities by manipulating the number of pore seeds, emphasizing the mechanical properties [29-31]. In terms of biological performance, Liang et al. demonstrated the superiority of the novel bone-mimetic design through in-vitro tests [32]. However, overall verifications, including in-vivo tests, are still lacking.

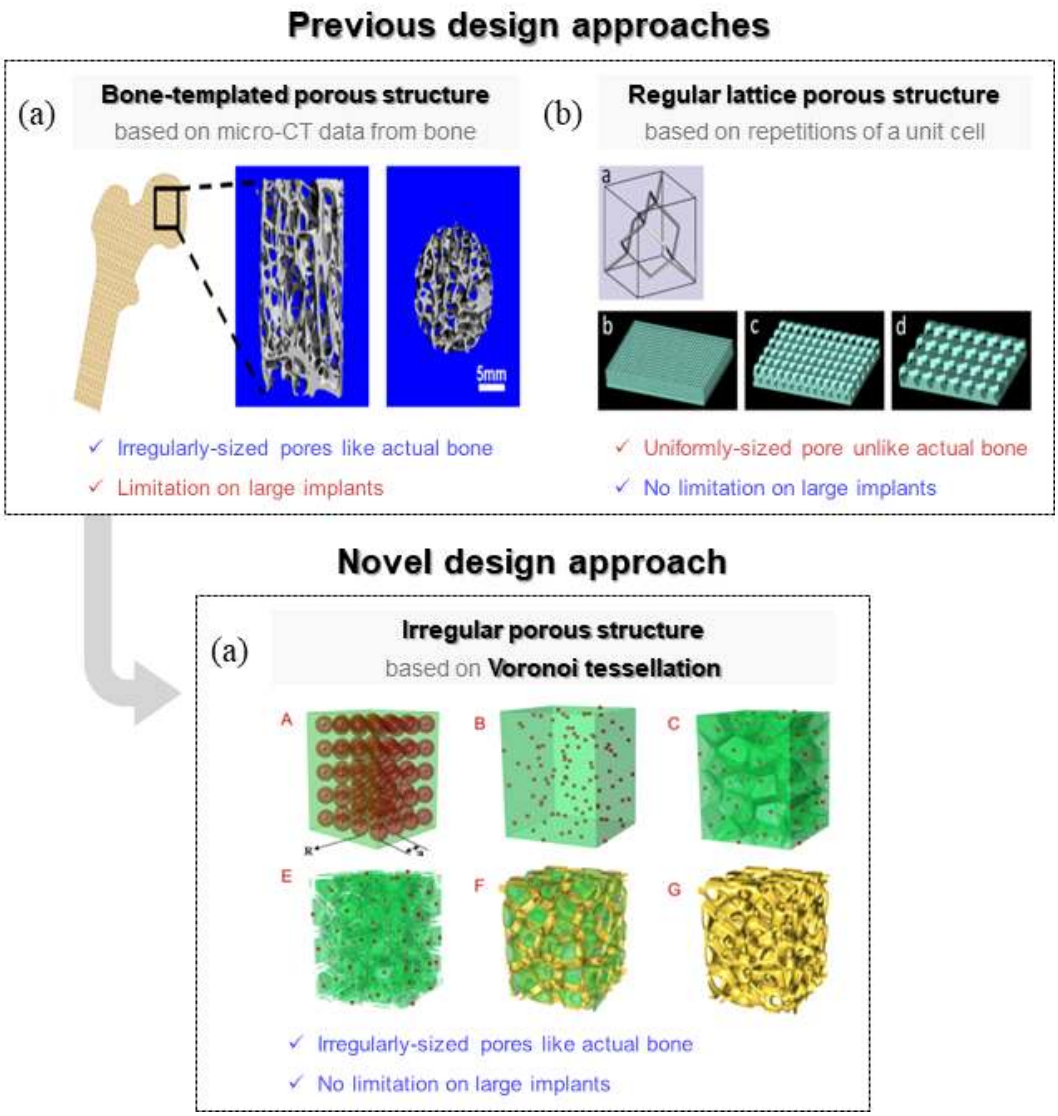

Figure 3. Design approaches for bone-mimetic porous structures: (a) using a bone template, (b) using a unit cell, and (c) employing Voronoi tessellation (the illustrations provided are from the literature [19, 23, 25]).

3. Challenges: optimizing the 3D printing process parameters

3D printing inherently demands fine-tuning of process parameters to ensure the desired product performance. In the SLM process, a laser scans the metal powder spread on a building bed along computed paths; this causes local melting and sintering of the powder and ultimately builds the final structure up by layer-by-layer repetitions [33]. Here, the process parameters, including laser power and scanning speed, are generally known to determine the product qualities [34-36].

Numerous researchers have devoted their efforts to achieving superior mechanical properties, fewer defects and reduced dimensional inaccuracies in solid products. For instance, Kaya et al. [37] found that an optimal combination of 80 W laser power, a scan speed of 1126.27 mm/s, and a hatch spacing of 45 μm yielded the best mechanical properties. Ferro et al. [38] demonstrated that specific energy densities between 40 and 100 J/mm^3 led to the highest specimen densities when varying laser powers (200 to 370 W) and scan speeds (30 to 120 ms in exposure time). Charles et al. [39] and Pal et al. [40] emphasized the importance of adjusting laser power and scan speed to minimize shape errors. In particular, the latter group suggested using weaker laser powers or faster scan speeds could be an effective strategy. While these initial establishments benefit bulk structure manufacturing, their applicability to complex porous structures remains uncertain.

The biological performance of porous structures relies on the pore sizes, which foster the formation of new bone and vascular tissue [41, 42]. Previous studies by Frosch et al. [43] and Fukuda et al. [44] indicated that pore sizes of 500 to 600

μm are ideal for cell ingrowth in titanium implants. Additionally, Taniguchi et al. [23], Ran et al. [45], and Ouyang et al. [46] supported these findings with in-vivo evidence, where around 600 μm pore sizes yielded the best fixation in rabbit bones. However, intense laser irradiation during the SLM process can reduce pore sizes [32, 45, 47-49], which may hinder vascularization if the pores become too small and then occluded [50, 51]. Therefore, selecting proper values of laser parameters and minimizing shape errors to preserve the original pore design will be vital to guarantee the expected functionality of the porous structure.

For mechanical properties, conventional solid orthopedic implants made from biocompatible metals display excessive strength and elastic modulus compared to bone [52, 53], leading to stress shielding, where the bone weakens [54]. Moreover, 3D-printed titanium, especially Ti6Al4V, often has poor ductility [55, 56]. Porous structures can mitigate these issues by being tailored to be weaker and more ductile than bulk materials [57, 58]. The related research underscores the importance of controlling the pore size and porosity to meet the adequate mechanical properties to be implanted [23, 29, 45, 48, 41, 59, 60]. However, as mentioned above, the SLM process can inadvertently shrink the pore size, decreasing the porosity. Limited studies have discussed the effects of laser power and scan speed on the porosity and internal defects in lattice scaffolds but have not extended their parametric observations to mechanical tests [61, 62]. Consequently, the relationship between laser-induced shape errors and mechanical properties in porous structures still needs to be systematically analyzed.

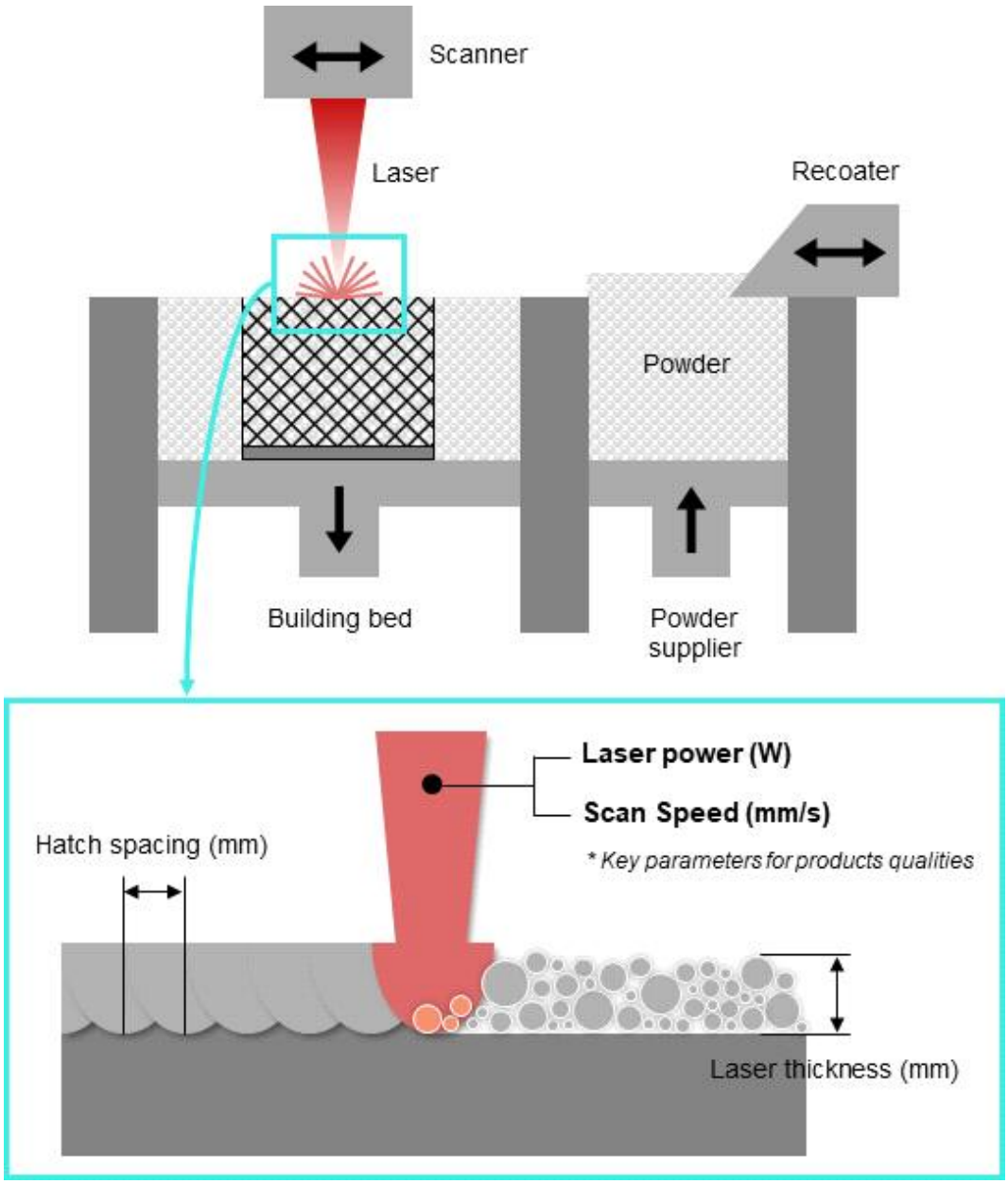

Figure 4. Schematic representation of the SLM process along with the laser parameters.

II. OBJECTIVES AND SCOPES

Overall, the current study focuses on the challenges associated with using 3D printing technology (especially SLM) to produce a complex porous structure. Specifically, we adopted a recent modeling technique of Voronoi tessellation to develop a bone-mimetic design and created a novel irregular porous structure. Before verifying the superiority in forming osseointegration, we fine-tuned the 3D printing (SLM) process parameters. This optimization work included fabricating Ti6V4Al specimens under different laser powers and scan speeds, characterizing pore shapes, and performing mechanical testing. Afterward, the qualified specimens from the optimized setting underwent animal implantation and histological analysis. We also prepared and examined the conventional bone-templated and regular lattice porous structures for comparison.

III. MATERIALS AND METHODS

1. Porous structure modelling

1.1 Irregular porous structure

The irregular porous structure was designed using commercial CAD software (Rhinoceros 3D, Robert McNeel & Associates, USA) and its Grasshopper plug-ins (ver. 1.0.0006). As shown in Figure 5, the modeling process involved a customized algorithm including the following steps: 1) Random scattering of points within a targeted area. 2) Voronoi tessellation. 3) Edge extraction from the generated diagram. 4) Smoothing of the edge corners. 5) Volumization to generate the final structure. For comparative analysis with the other designs, the porosity and strut thickness were set to 62.85% and 150 μm, respectively. In particular, as shown in Figure 6, the resulting pore sizes were determined by inscribing spheres inside the pores and found to be normally distributed, with an average of 600.77 μm and a standard deviation of 49.62 μm.

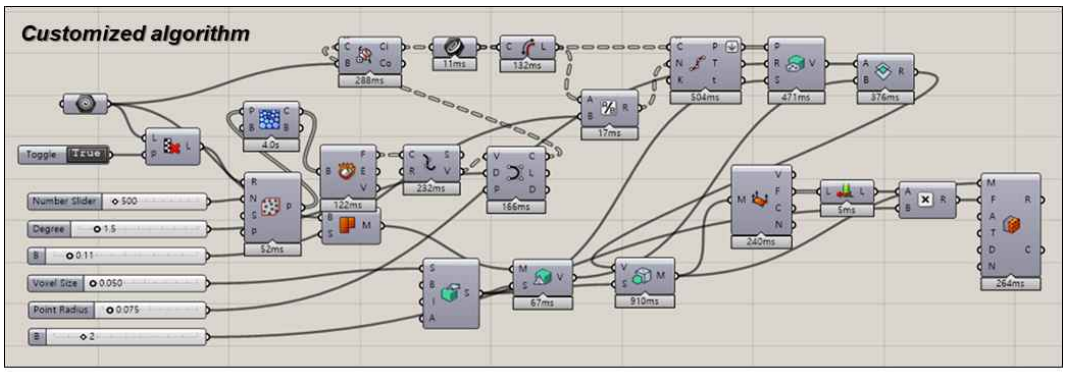

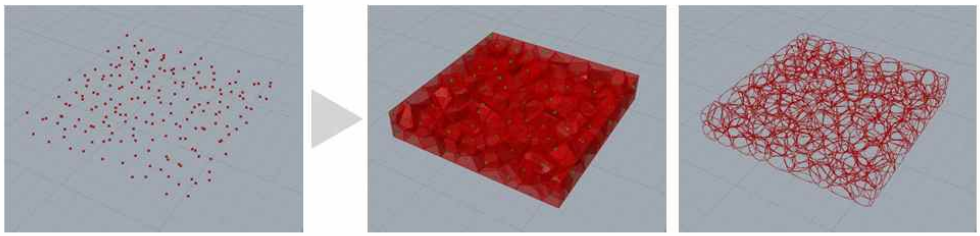

1. Random scattering of points 2. Voronoi tessellation 3. Edge extraction

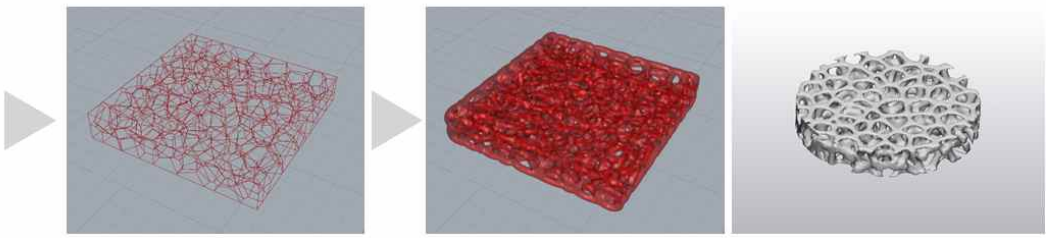

4. Smoothing of the edge corners 5. Volumization to generate the final structure

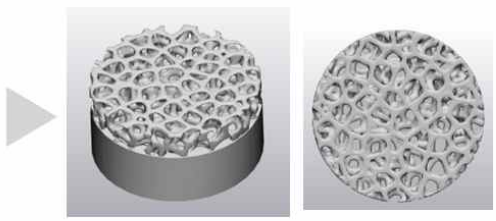

6. Specimen model

Figure 5. Modeling of irregular porous structure.

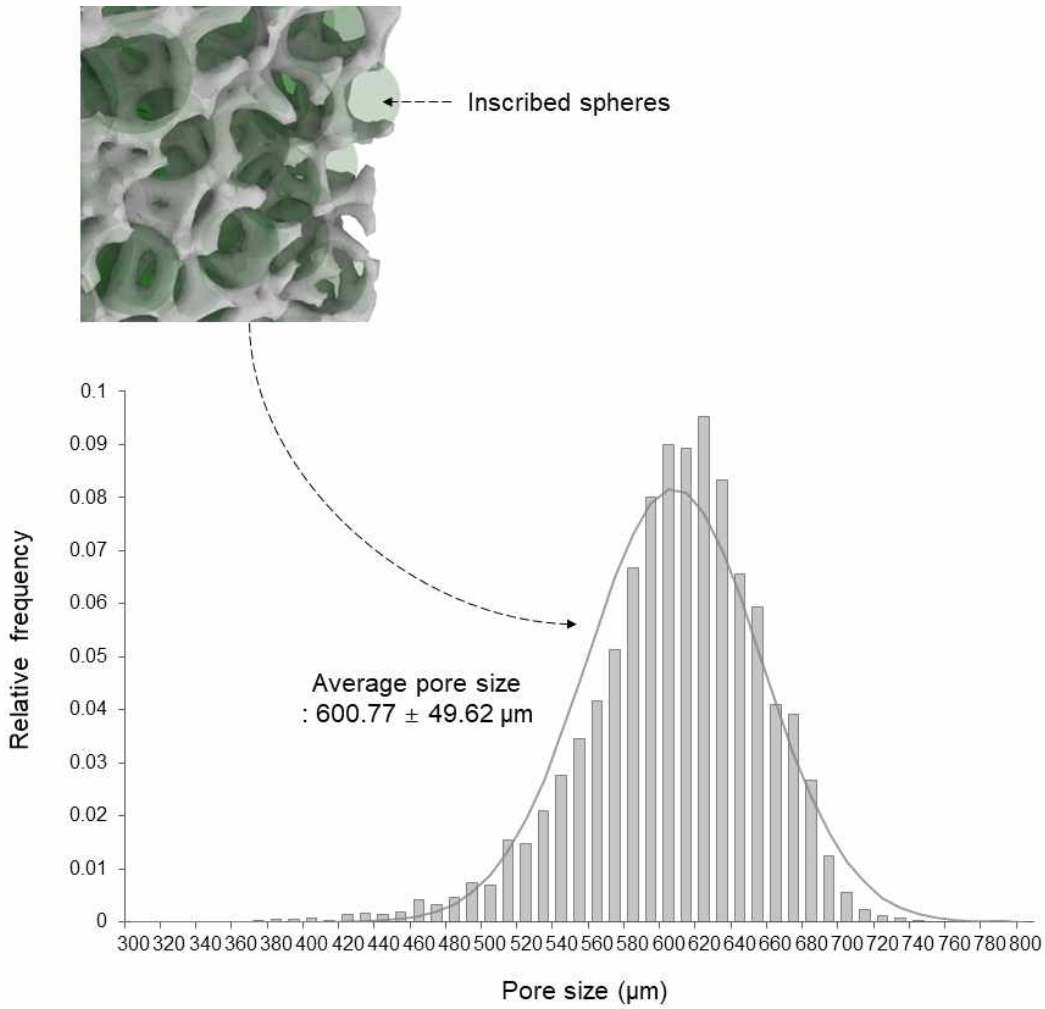

Figure 6. Designed pore size distribution of irregular porous structure.

1.2 Bone-templated porous structure

A rabbit's distal femur was scanned using a micro-CT system (TVX-IMT225-RC-S2, Tech Valley, Korea). Subsequently, the cancellous bone area was reconstructed and then tailored using commercial image processing and computer-aided design (CAD) software (Mimics 22.0 and 3-matic 14.0, Materialise, Belgium), as shown in Figure 7. The porosity and strut thickness of the bone template were measured to be 62.75% and 150 μm, respectively, and were used as references in the other designs in this study.

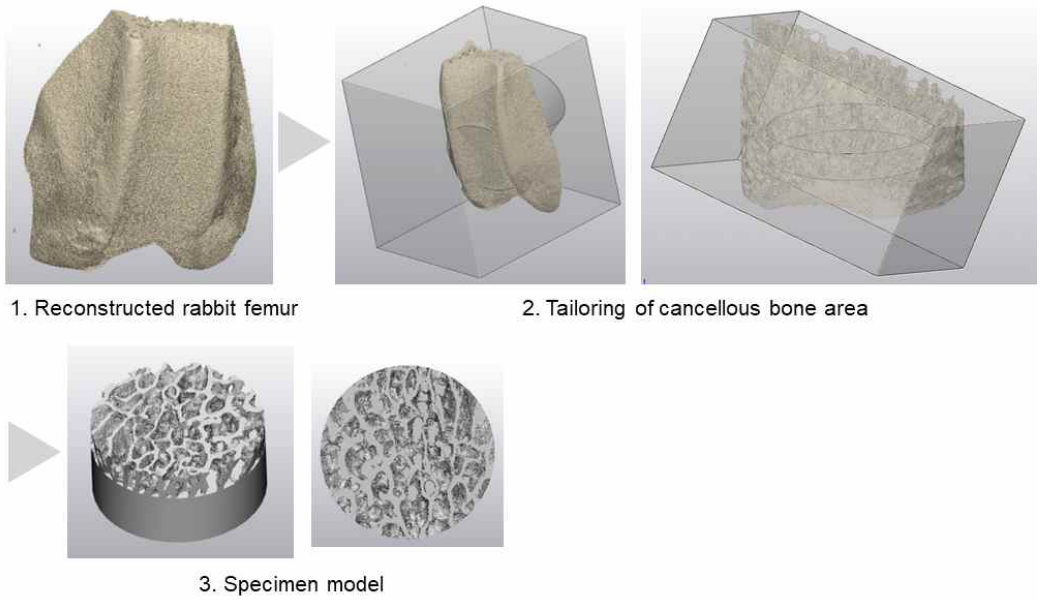

Figure 7. Modeling of bone-templated porous structure.

1.3 Regular lattice porous structure

Using the same commercial computer-aided design (CAD) software mentioned in 1.1., a lattice porous structure was created by packing diamond crystal unit cells within a targeted area, as shown in Figure 8. For comparative analysis with the other designs, the porosity and strut thickness were set to 63.51% and 150 μm, respectively.

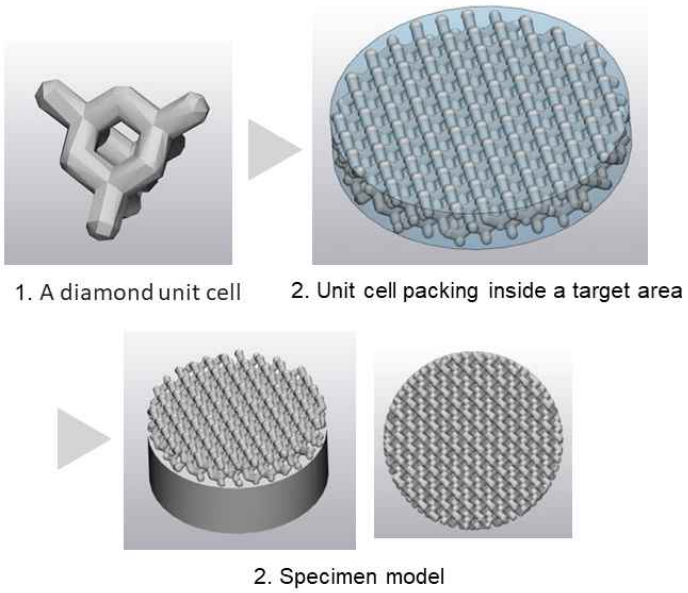

Figure 8. Modeling of regular lattice porous structure.

2. Specimen fabrication

Ti-6AI-4V grade 23 powder, with a particle size ranging from 15 to 45 μm (TEKMAT™, Tekna, Canada), was utilized for the 3D printing process. As Table 1 from the datasheet shows, the material adhered to an international standard (ASTM F3001) regarding its chemical composition, featuring an extra-lowered content of interstitial elements, including O, N, H, C, Fe, and Y.

Table 1. The chemical composition of the Ti-6Al-4V Grade 23 powder utilized in this study (expressed in weight percentage).

Ti	Al	V	O	N	H	C	Fe	Y	Other
Bal.	6.39	4.07	0.08	0.014	0.002	< 0.005	0.13	< 0.001	< 0.1

The specimens were produced using an SLM machine (MetalSys 150E, Winforsys, Korea), following the manufacturer's guidance for manipulating the process parameters within the allowed ranges. Specifically, for parametric study specimens, the laser power and scan speed varied at 80-160 W and 550-950 mm/s, respectively, while the others remained constant. For in-vivo test specimens, the subsequently selected set of process parameters were used (laser power = 80 W, scan speed = 950 mm/s, hatch spacing = 0.07 mm, and layer thickness = 0.03 mm). Table 2 and 3 provide information on the process parameter settings used and their energy densities calculated as below:

$$Energy\ density\ =\ \frac{Laser\ power}{Scan\ speed\ \times\ Hatch\ spacing\ \times\ Layer\ thickness} \quad (1)$$

For dimensions, the specimens for the parametric study were prepared to be cuboids with a length of 10 mm, a width of 10 mm, and a height of 5 mm and cylinders with a diameter of 10 mm and a height of 10 mm as shown in Figure 9. Also, the specimens for the in-vivo test were prepared to have a 6 mm diameter and 1 mm thickness, as shown in Figure 10.

Table 2. SLM process parameter settings used for parametric study specimens.

No	Laser power (W)	Scan speed (mm/s)	Hatch spacing (mm)	Layer thickness (mm)	Energy density (J/mm3)
1	160	950	0.07	0.03	80.20
2	140	950	0.07	0.03	70.18
3	120	950	0.07	0.03	60.15
4	100	950	0.07	0.03	50.13
5	100	750	0.07	0.03	63.49
6	100	550	0.07	0.03	86.58
7	80	950	0.07	0.03	40.10
8	80	750	0.07	0.03	50.79
9	80	550	0.07	0.03	69.26

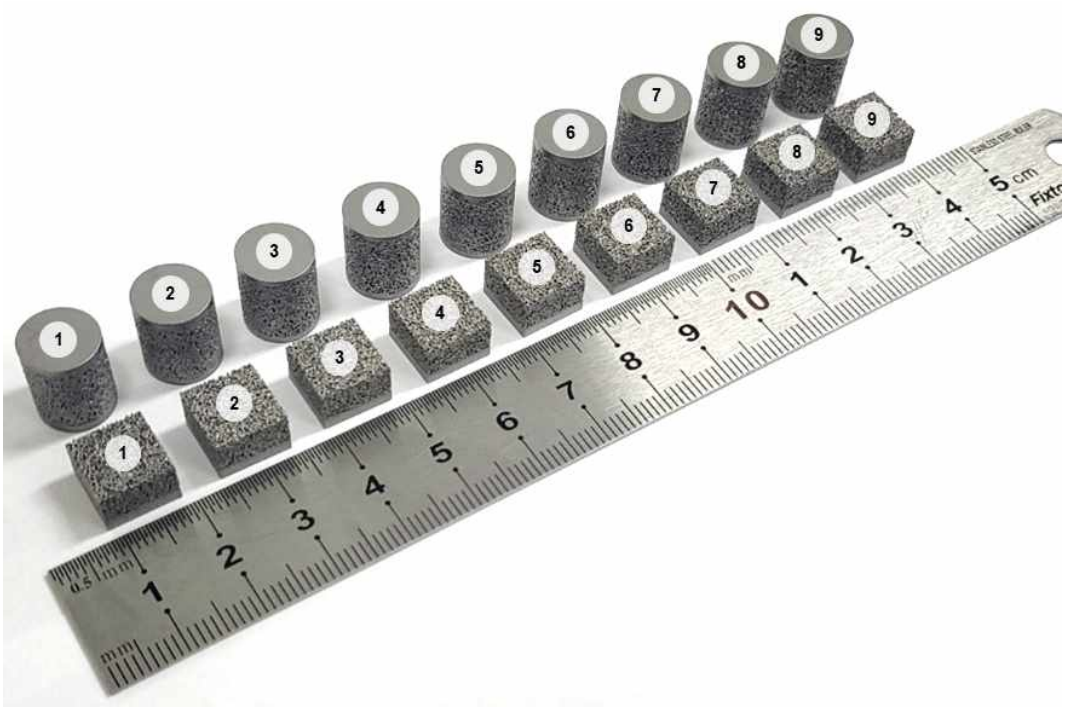

Figure 9. As-built parametric study specimens.

Table 3. SLM process parameter settings used for in-vivo test specimens.

No	Laser power (W)	Scan speed (mm/s)	Hatch spacing (mm)	Layer thickness (mm)	Energy density (J/mm3)
7	80	950	0.07	0.03	50.13

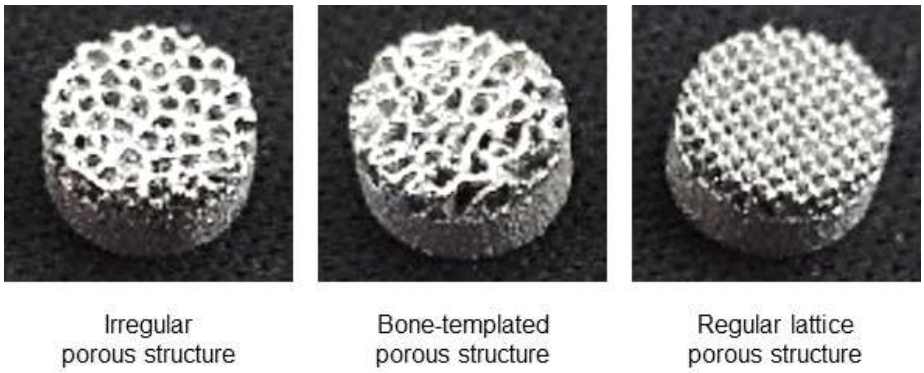

Figure 10. As-built in-vivo test specimens.

3. Pore shape characterization

As shown in Figure 11, the cuboid specimens were scanned utilizing a micro-computed tomography (micro-CT) system (Xradia 620 Versa, Carl Zeiss, Germany) while positioned on a rotating stage. Each scan generated 1,017 sliced images with a voxel size of 1.5 μm. The acquired data were converted into 3D-reconstructed models using commercial image processing software (Mimics, Materialize, Belgium). This software allowed for cross-sectional analysis and provided the ability to draw fitting circles within the pores to measure their diameters, as shown in Figure 12. Over 500 individual pores were measured for each observation plane (side and top views), and the shape error was calculated as below:

$$Shape\ error = Average\ pore\ size - Mean\ pore\ size \quad (2)$$

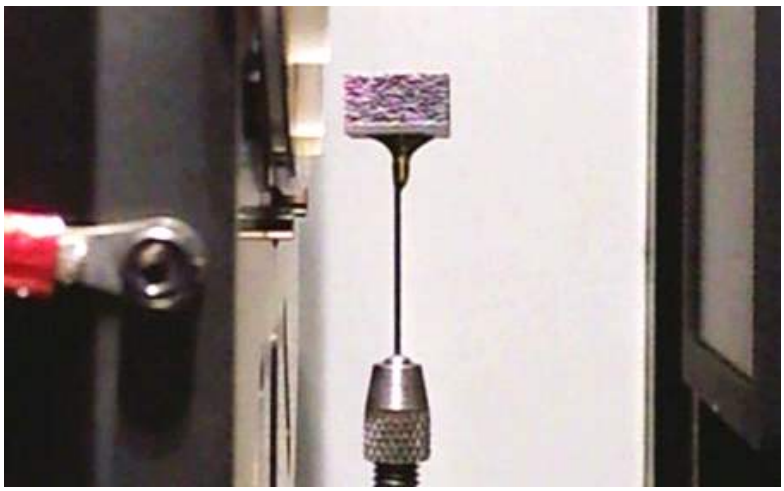

Figure 11. Micro-CT scan of the specimen.

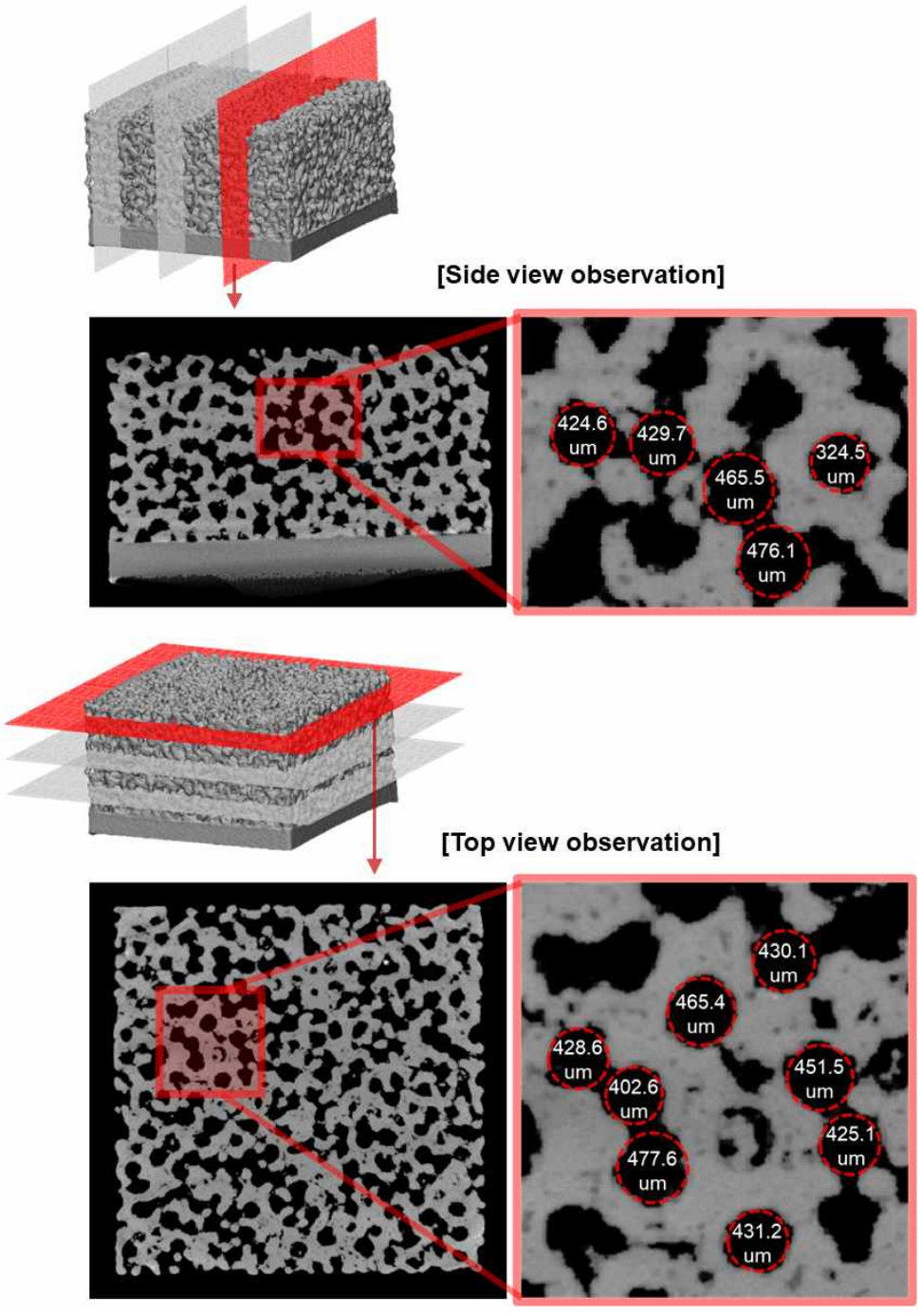

Figure 12. Pore size measurements in each observation view.

4. Mechanical testing

The compression tests were performed in accordance with ISO 13314:2011(E). The cylindrical specimens were subjected to quasi-static loading at a consistent 1 mm/min rate utilizing a universal testing machine (AG-Retrofit-250kN, Shimadzu, Japan). A minimum of five specimens were tested for each experimental group. The compressive strength, elastic modulus, and energy absorption of the produced porous structures were obtained from the stress-strain curves based on the specifications in the aforementioned standards.

5. Animal implantation

5.1 Animal preparation

Thirty-six-week-old female New Zealand white rabbits with an average weight of approximately 4 kg were for animal implantation. The rabbits were housed individually in a controlled environment with a temperature of 23 ± 2 °C, a humidity of 60% ± 10%, and a 12-hour light cycle. They had ad libitum access to food and water. All in-vivo tests were conducted using the National Institutes of Health guide for the care and use of laboratory animals and the ARRIVE guidelines. Also, all experimental protocols were approved by standards issued by the Ethics Committee on Animal Experimentation at Samsung Medical Center. (SMC 2018-0713-002). Thirty-nine rabbits were arranged into three groups: the bone-templated porous structure group (n=7 for two-week implantation and n=6 for six-week implantation), the regular lattice porous structure group (n=7 for two-week implantation and n=6 for six-week implantation), and the irregular porous structure group (n=7 for two-week implantation and n=6 for six-week implantation).

5.2 Animal preparation

The surgical procedure in this study is presented in Figure 13. General anesthesia was induced by intramuscular injection of ketamine (700 μL/kg) and xylazine hydrochloride (200 μL/kg). The right knee of each rabbit was shaved and sterilized with povidone-iodine. While in the supine position, longitudinal incisions

were made on the right legs, starting from 2 cm above the knee joint and extending to 1.5 cm below. The vastus medialis muscle was cut on the upper inner side of the patella, extending through the patella and patella tendon to the upper end of the tibial tuberosity, allowing the patella to move to the outer side. A 6 mm hole was then created in the upper part of the trochlear groove using a trephine burr while the reaming process was performed gently and carefully. During the reaming procedure, we sprayed normal saline to prevent thermal injuries around the bone and soft tissue. Then, we placed an experimental specimen in the hole of the trochlear groove with the porous surface facing the cancellous bone and gently impacted the specimen to ensure thorough contact with the bone. Following implantation, patella reduction was performed, and the knee motion was checked. Afterward, the joint capsule and subcutaneous tissue were sutured with Vicryl 2-0, and finally, the wound was disinfected with povidone-iodine.

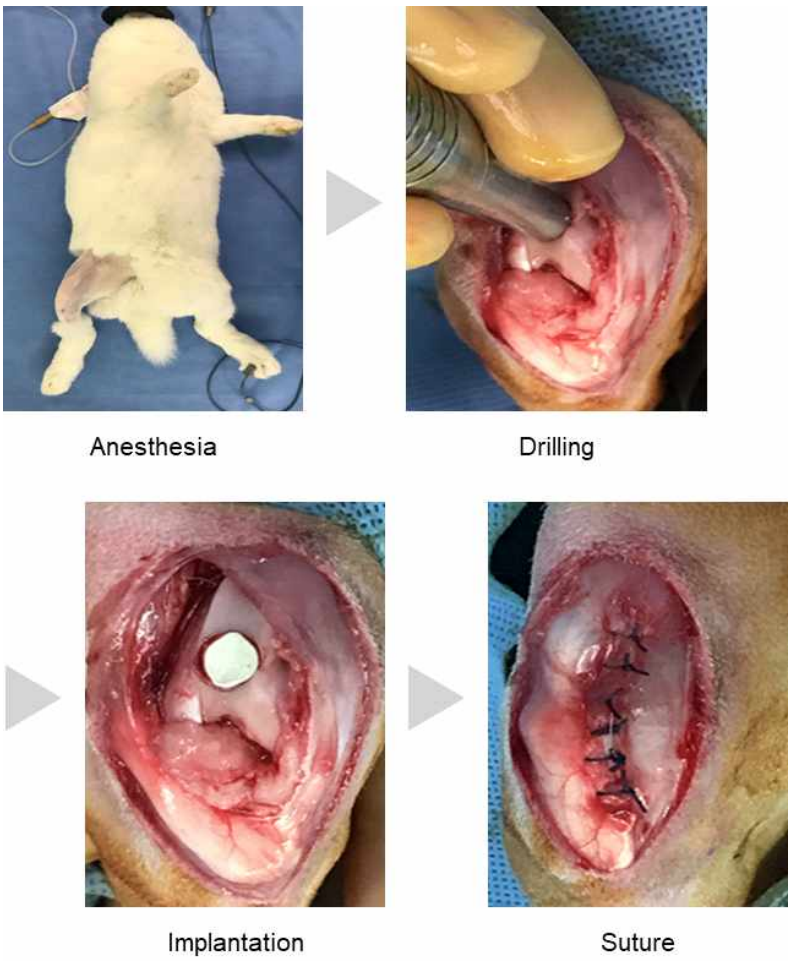

Figure 13. Surgical procedure for animal implantation.

5.3 Postoperative care and sacrifice

Following the surgical procedure, the rabbits received an intramuscular administration of 0.6 mL/kg of cefazoline (Chongkundang, Korea) and 1.8 mL/kg of ketoprofen (UNIBIO tech, Korea). The rabbits were allowed to move freely within their cages and sacrificed two or six weeks after implantation. The euthanasia process involved an intramuscular injection of ketamine (700 μL/kg) and xylazine hydrochloride (400 μL/kg), followed by an intravenous injection of potassium chloride. Subsequently, the distal femurs were carefully harvested, placed in 10% neutral buffered formalin (Sigma-Aldrich Corp, USA), and fixed for two weeks.

6. Histological analysis

6.1 Slide preparation and staining

The specimens were cleaned with distilled water and decalcified using an ethylenediaminetetraacetic acid solution with pH 9.0 (Zytomed Systems GmbH, Germany) for five weeks. Once the removal of calcium was confirmed, the specimens were embedded in paraffin and cut into 50 μm thick sections using a hard tissue slicer (Struers, Germany). The obtained sections were dyed using Masson's trichrome staining kit (Sigma-Aldrich, USA) technique to visualize the contact surface and osseointegration.

6.2 Bone histomorphometry

Optical images were captured using a digital camera attached to a microscope (CC-12, Soft Imaging System GmbH, Germany) with ×12.5 and ×100 objectives (BX51, Olympus, Tokyo, Japan). We employed the bone histomorphometry methodology described in a previous study [63], as shown in Figure 14. Specifically, a professionally skilled investigator analyzed the images based on the following. 1) Bone-to-implant contact (BIC), the percentage of the direct contact surface between mineralized bone and the porous structure. 2) Absent area, the percentage of the non-contact area within the total area in a 1000 μm distance. 3) Bone area, the percentage of new bone formation and neovascularization area within the total area in different distances of 500, 1000, and 2000 μm.

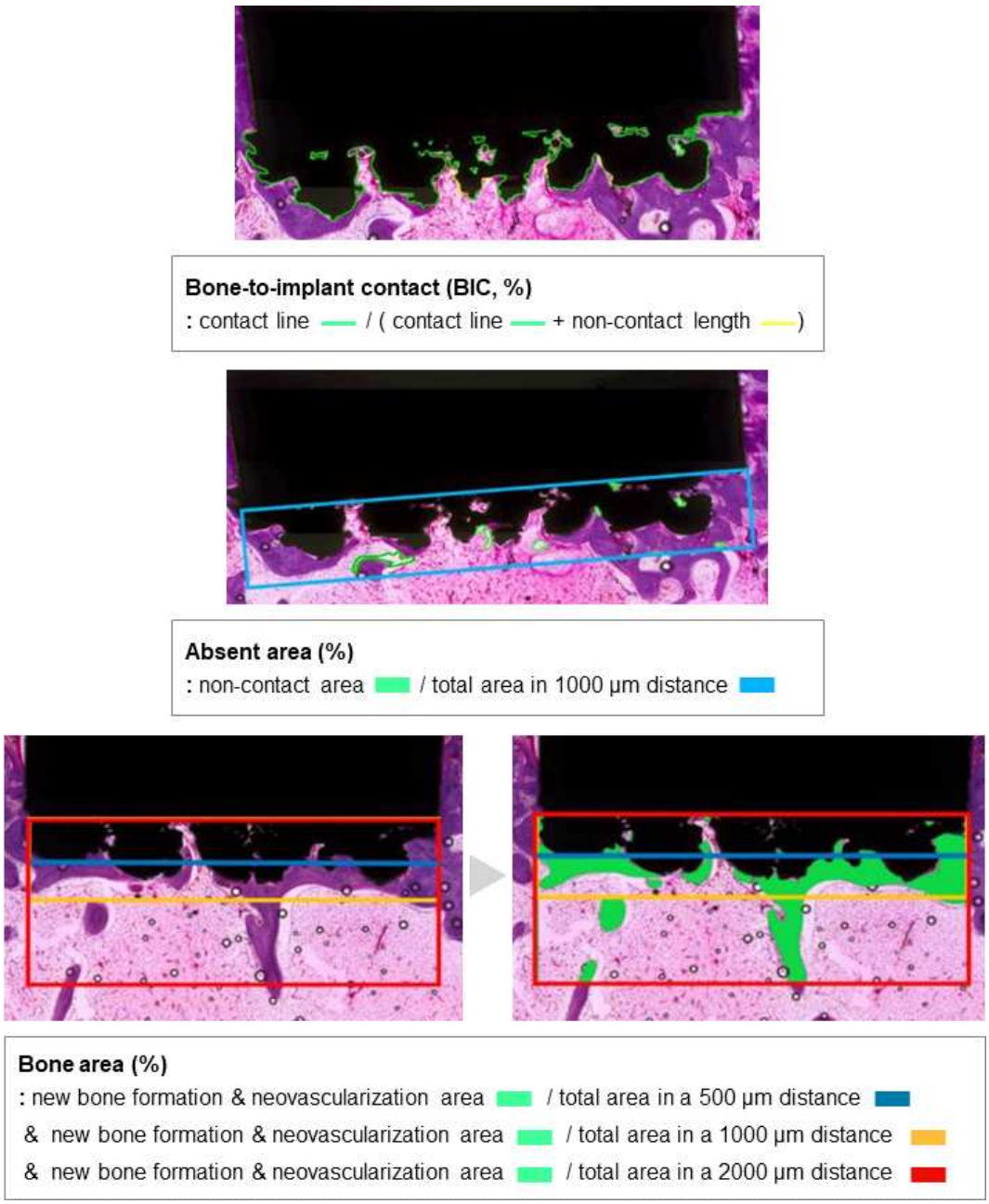

Figure 14. The process of bone histomorphometry from previous study [63].

7. Statistical analysis

Statistical analyses were conducted using commercial statistical software (SPSS 28.0, IBM, USA) to ascertain significant differences among the groups. A one-way analysis of variance (ANOVA) was employed, followed by Tukey's post-hoc tests. Statistical significance was established at a p-value threshold of less than 0.05.

IV. RESULTS AND DISCUSSION

1. Minimization of pore shape error in SLM manufacturing

During the process of SLM, a laser serves as the energy source to melt powder layers along predetermined paths [33-35]. Multiple researchers have proposed that: 1) the micro-sized struts within the porous structure have limited energy capacity; 2) as a result, excessive energy can propagate out of the paths when irradiated by the laser; 3) ultimately, the surrounding powder can heat up and adhere to the solidified strut surface, narrowing the pores [32, 47, 61]. Concerning this, the energy supplied to the struts is generally associated with the volumetric energy density, which is proportional to the laser power and inversely proportional to the scanning speed (see equation (1)). Simply using a weaker laser power or faster scan speed can lead to thinner struts, resulting in diminished error in pore size.

The trends observed in our results support the above. Figures 15-17 demonstrate how the pore size distributions deviated from the designed one according to different parameter settings. Also, Figures 18-19 show the shape errors along with the visualized pore shape changes based on the reconstructed 3D models. Specifically, adjusting the laser power from 160 W to 80 W with a constant scan speed of 950 mm/s led to a gradual reduction in shape error. The shape error decreased from 288.88 μm to 149.05 μm in the side view and from 239.15 μm to 135.65 μm in the top view (see Figure 15). Furthermore, the shape error progressively decreased when the scan speed went from 550 mm/s to 950 mm/s while maintaining a constant laser power of 100 W. The side view error fell from

218.14 μm to 185.39 μm, while the top view error went from 203.05 μm to 149.05 μm (see Figure 16). Similarly, the same changes in scan speed at a reduced laser power of 80 W caused the shape error to steadily decrease from 206.29 μm to 159.17 μm in the side view and from 188.78 μm to 159.17 μm in the top view (see Figure 17). Consequently, the combination of the weakest laser power (80 W) and the fastest scan speed (950 mm/s) presented minimized shape errors. By the way, the shape errors were more significant at stronger laser powers than at slower scan speeds. For instance, the parameter settings 140 W – 950 mm/s and 80 W – 550 mm/s had nearly equal energy densities (70.18 J/mm³ for the former and 69.26 J/mm³ for the latter, as shown in Table 2). However, the first setting resulted in smaller pores—by 26.67 μm in the top view and 54.21 μm in the side view—compared to the other setting (see Figures 18-19).

One notable finding was that the shape errors observed from the side were consistently greater than those from the top. The effect of the overhang angle likely explains this. In 3D printing, it is recommended to install support structures in regions where the horizontal angle to the building bed is less than 45 degrees. The lack of adequate support typically leads to dimensional inaccuracies [64]. Generally, such overhang features are prone to distortion in the building direction by residual stresses during the cooling phase and gravitational forces [65-67]. Moreover, regarding porous structures, some studies have indicated that the struts tend to accumulate poorly melted powder on their bottom surfaces while fabricated on a loose powder layer [68-70]. For example, Bertocco et al. [70] utilized the SLM process to produce a lattice scaffold of overhang-angled unit cells. The struts appeared bent downward, showing coarse satellite powder adhering to their

bottoms. Also, these observations were more apparent when viewed from the side rather than the top.

The current study investigated irregular porous structures that highly mimicked cancellous bone, characterized by randomly interconnected pores. The intricate design inevitably contained a considerable number of overhang struts, as schematized in Figure 20. Therefore, we present the following assumptions: 1) The shape error induced by energy diffusion primarily affected the geometric discrepancies in pore size, determining the overall trend according to the various parameter settings. 2) The shape error from overhangs contributed secondarily, causing the differences that depend on the measurement planes. Supplementary data in the appendix further supports this based on the results from optical observations (see Figures A1-A2).

Another important point is that the extra shape error, likely caused by overhang struts, was more pronounced at stronger laser power settings. Specifically, at a setting of 80 W – 950 mm/s, the difference in shape error between the side and top views was 13.4 μm, but at a setting of 160 W – 950 mm/s, it was 47.65 μm (see Figure 15). In contrast, reducing the scan speed to a slower level did not significantly affect the discrepancy between the two views. Briefly, despite reducing the scan speed from 950 to 550 mm/s while maintaining a constant laser power of 100 W, the difference even decreased from 26.22 to 11.85 μm (see Figure 16). Similarly, no distinct trend was found under the manipulation of scan speed at a constant laser power of 80 W (see Figure 17).

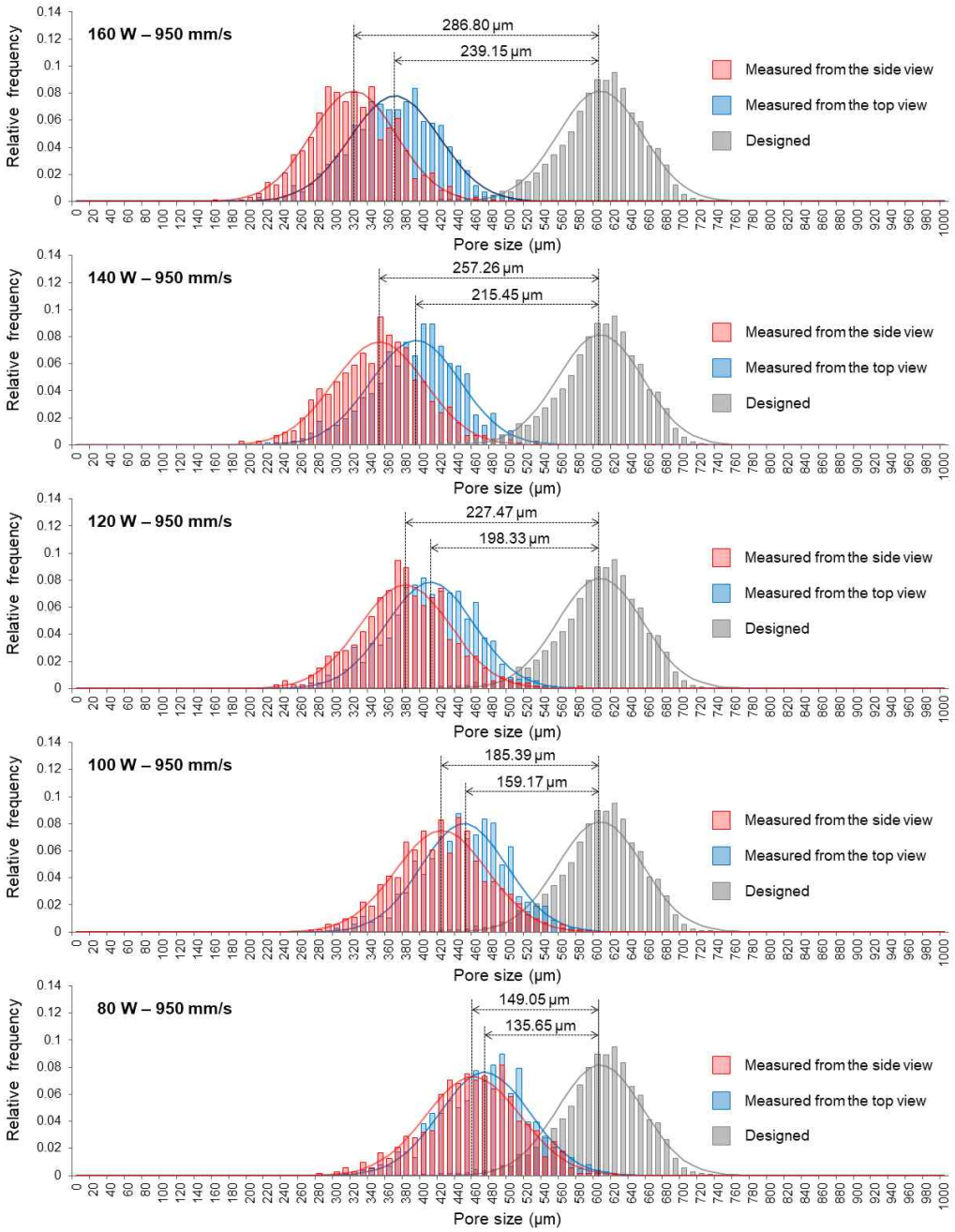

Figure 15. Pore size distributions at various laser powers (160-80 W) at a constant scan speed of 950 mm/s.

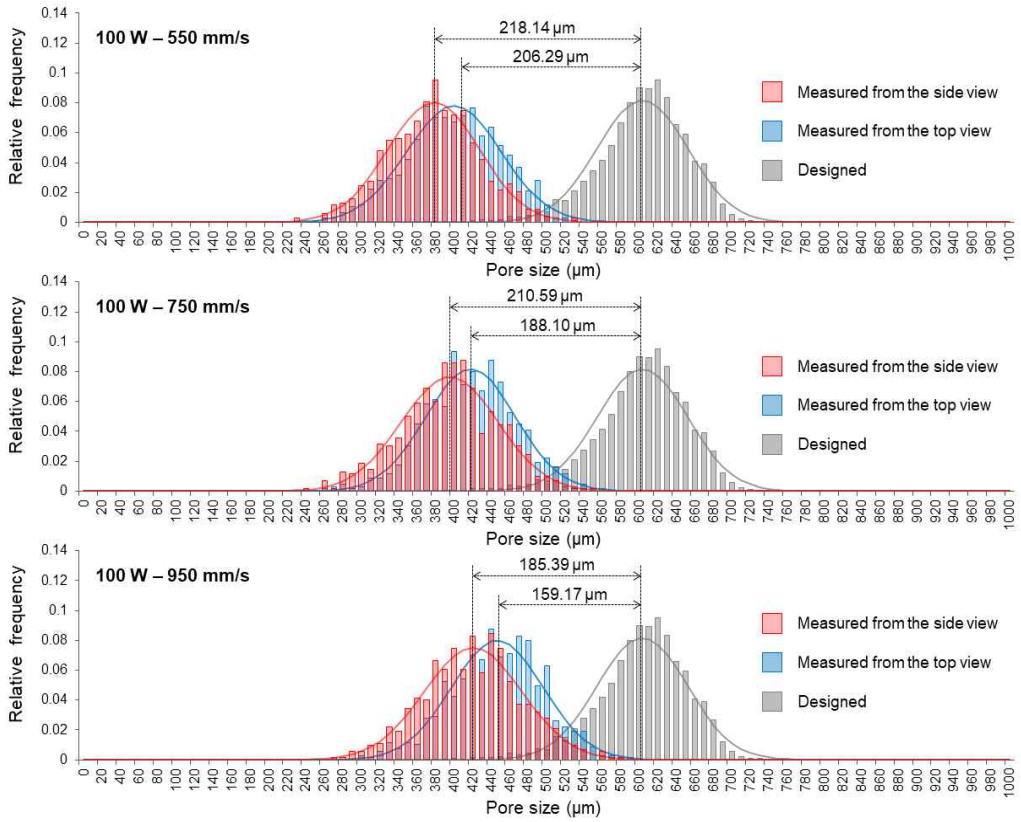

Figure 16. Pore size distributions at various scan speeds (550 – 950 mm/s) at a constant laser power of 100W.

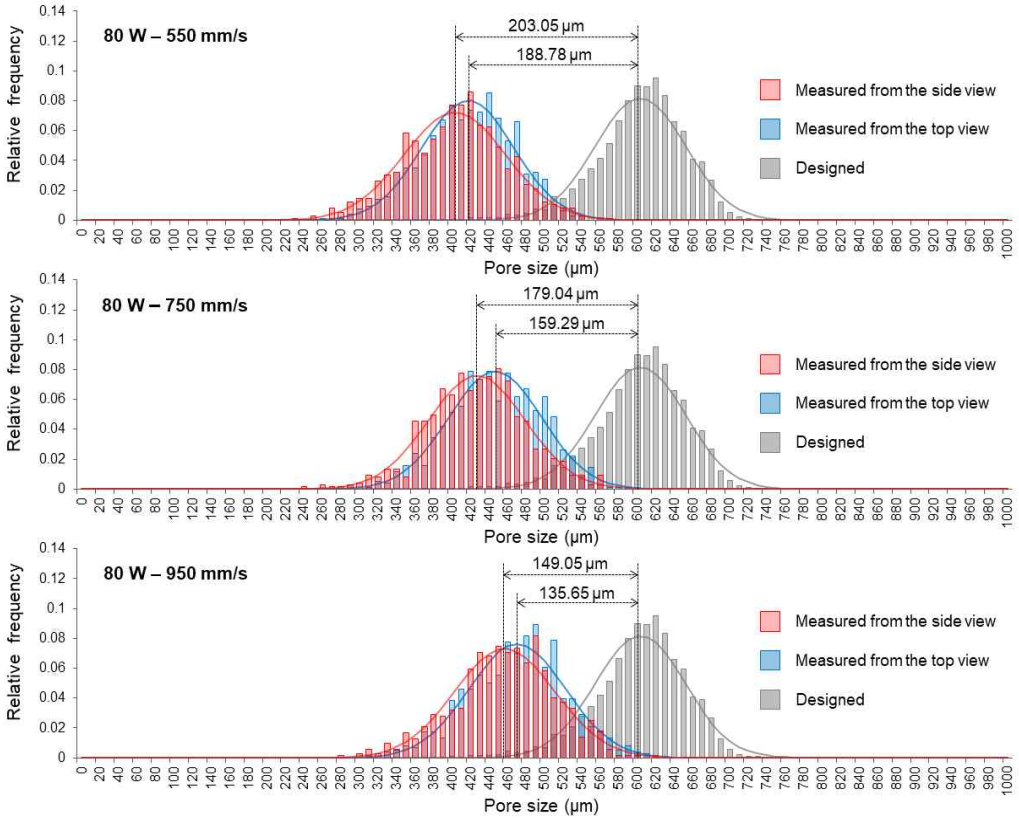

Figure 17. Pore size distributions at various scan speeds (550 – 950 mm/s) at a constant laser power of 80W.

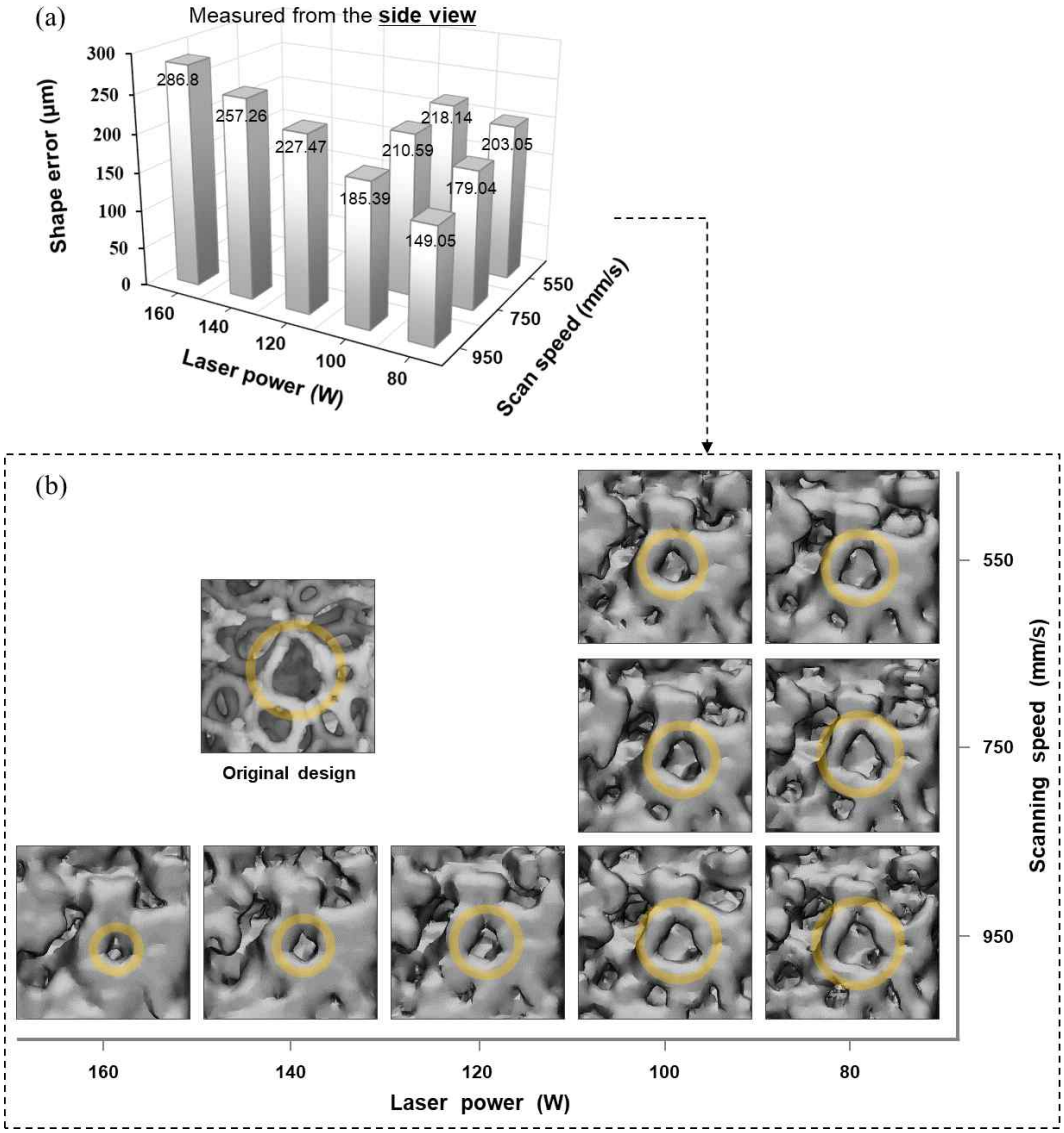

Figure 18. (a) Shape errors observed from the side view for various parameter settings; (b) Visualization of changes in pore shape based on the 3D-reconstructed models.

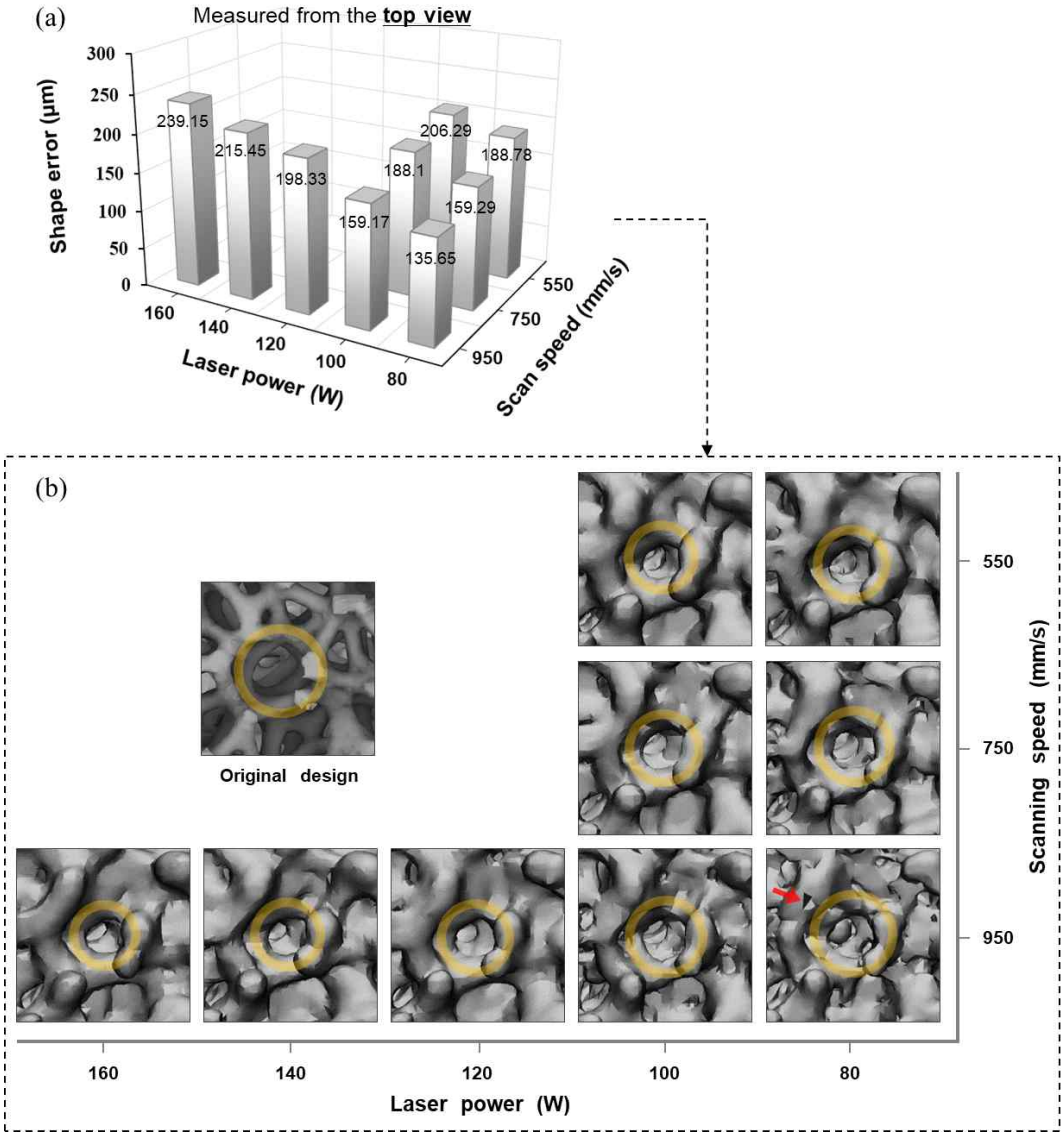

Figure 19. (a) Shape errors observed from the top view for various parameter settings; (b) Visualization of changes in pore shape based on the 3D-reconstructed models.

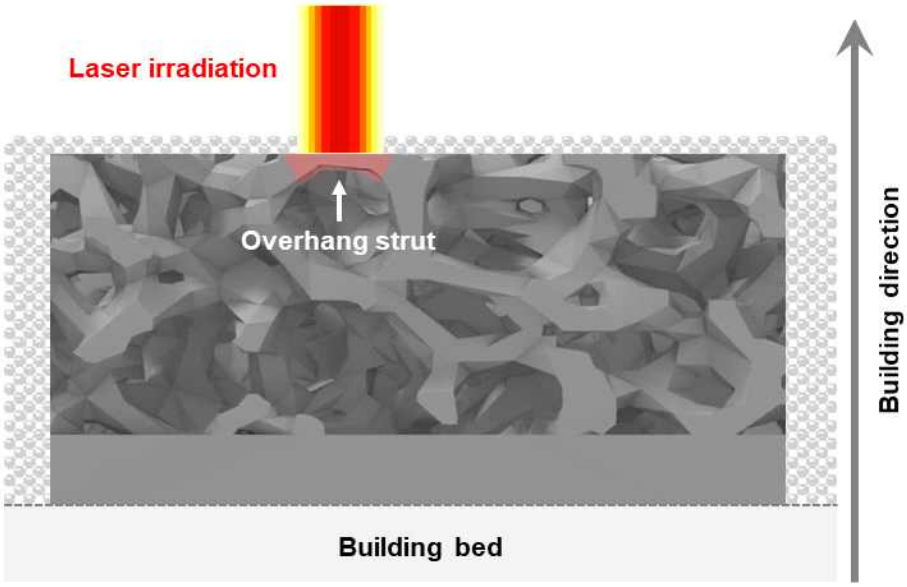

Figure 20. A schematic depicting how each pore in an irregular porous structure can be susceptible to overhang-induced shape error during the SLM process.

2. Determination of mechanical properties by pore shape error

Our findings from the compression tests reveal a clear correlation between the shape error and mechanical properties of porous structures under varying laser parameters. Simply put, the obtained compressive strength and elastic modulus tended to increase with a rise in shape error (see Figures 21-22 along with Figures 18-19). This relationship was particularly evident when the specimens were viewed from the top. For instance, the specimens produced at 100W – 550 mm/s exhibited better mechanical properties than those produced at 120W – 950 mm/s. In porous structures, the struts bear the applied load [71], and the shape error addressed in this study pertains to the narrowing of the pores, which indicates an increase in strut thickness. Thus, the former setting should have resulted in greater shape errors; however, this was only reflected in the results from the top view. As illustrated in Figure 23, the scatter plots show that the coefficient of determination between each mechanical property and the top-view measurements is closer to 1 compared to the other. Combined with the assumptions in 3.1, this suggests that the overhang-indued shape errors probably had a lesser impact on the load-bearing capacity than the thickening of struts due to energy propagation.

Another noteworthy fact is that shape error is not the only factor affecting compressive strength in response to different parameter settings. By downregulating the laser power from 160 to 80 W with a scan speed of 950 mm/s, the shape error fell by approximately 43-48%. However, the compressive strength more sharply dropped by approximately 66% (see Table 4). In addition, with the upregulation of the scan speed from 550 to 950 mm/s at a laser power of 100 W

or 80 W, the shape error decreased by approximately 15-28%%. However, the compressive strength led to a more significant decrease of approximately 41-43% (see Tables 5-6). Some previous studies have identified lack-of-fusion defects within the pore struts, attributing these issues to poor energy inputs influenced by laser power and scan speed [61, 62]. Indeed, in our findings, the specimen produced at a setting of 80 W–950 mm/s—yielding the lowest energy density—exhibited defects on the surface of the struts (see the red arrow in Figure 19 (b)). Consequently, the process-inherent defects and shape errors likely played a role together in the initial failure of the strut after the elastic deformation, affecting the compressive strength. Notably, the occurrence of the process-inherent defects in the struts appeared somewhat independent of that in the bulk solid body, as shown in supplementary data in the appendix (see Figure A3).

This study's porous structures possessed sufficient compressive strengths for implantation, ranging from 131.45 to 390.38 MPa, compatible with or surpassing that of cortical bone (~200 MPa) [72, 73]. Furthermore, the elastic moduli were obtained from 6.24 to 10.6 GPa, which are between the known maximums of cortical bone (~17 GPa) and cancellous bone (~3.8 GPa) [73-75]. These intermediate values could be beneficial for orthopedic implants in avoiding stress shielding, as actual bone consists of both bone types.

Meanwhile, Figure 24 indicates that excessive shape errors in porous structures can abruptly halt plastic deformation. Under the quasi-static loading condition, the stress-strain curve for porous structures generally starts from the elastic deformation phase and transitions to the plateau phase. Due to strut buckling and subsequent layer-by-layer collapse, the stress remains relatively steady at 60-70%

strain in the plateau phase and then rises sharply in the densification phase [70, 71]. However, in our study, the plastic deformations of the specimen produced at stronger laser powers of 140-160 W and a constant scan speed of 950 mm/s were terminated without visible densifications (see Figure 24 (a)). The results matched those in previous works since the parameter settings yielded substantial dimensional inaccuracies. Luo et al. [76] found that 3D-printed porous structures with thicker struts faced catastrophic failures resulting in brittle cracking, whereas the others with thinner struts experienced a more gradual compaction. Likewise, Gao et al. [49] observed that lattice scaffolds with narrower pores suffered from 45-degree shear fractures, while those with wider pores underwent plastic collapse. Returning to the current study, lowering the laser power to 80-120 W at the same scan speed extended the plateau phases and reduced shape errors (see Figure 24 (a) along with Figure 15). In contrast, modulating the scan speed to narrow the pores and thicken the struts tended to result in early failure again (see Figure 24 (b) along with Figure 16).

In general, while cancellous bone is considerably weaker than cortical bone, it has a sufficient plateau phase and excellent energy absorption capacity, enabling it to withstand high-impact situations [77, 78]. Hence, there is a significant demand for porous orthopedic implants to fulfill this essential role [79, 80]. In this respect, Figure 25 denotes that the processing parameters in selective laser melting (SLM), particularly laser power, need to be correctly optimized to maximize energy absorption potential. In any case, all tested specimens showed energy absorptions at least five times greater than that of cancellous bone (see Figure 25 (a-c)). Considering that actual bone can self-repair over its lifetime [81], this

notable difference in energy absorption seems crucial for ensuring long-term durability for a substitution.

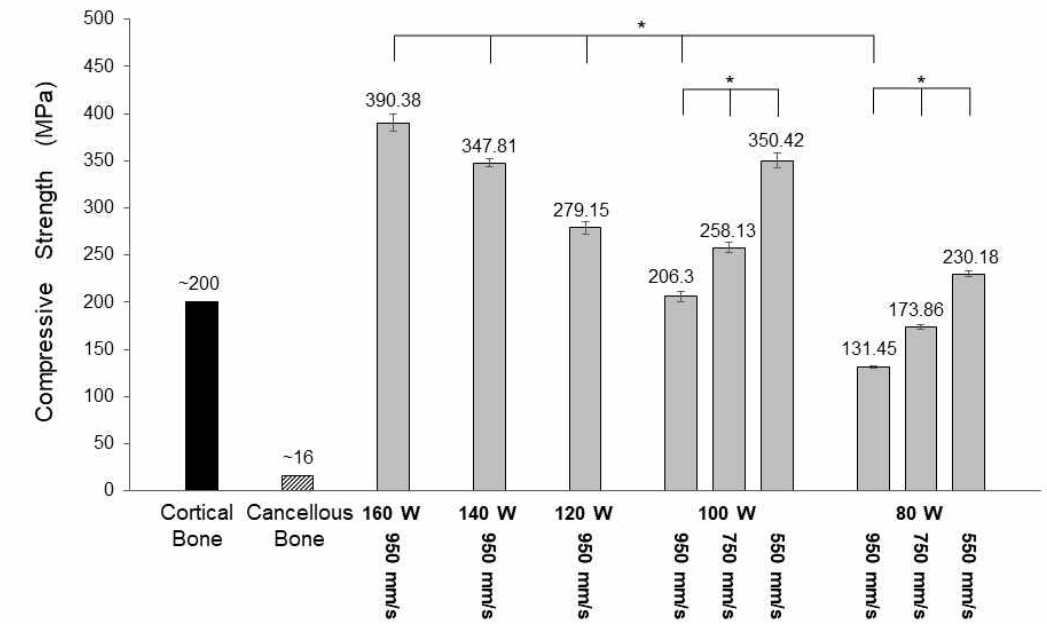

Figure 21. Compressive strengths of the specimens produced under various parameter settings (information for actual bone is sourced from the literature [72-75]). The results are presented as mean ± standard deviation with asterisks denoting $P < 0.05$.

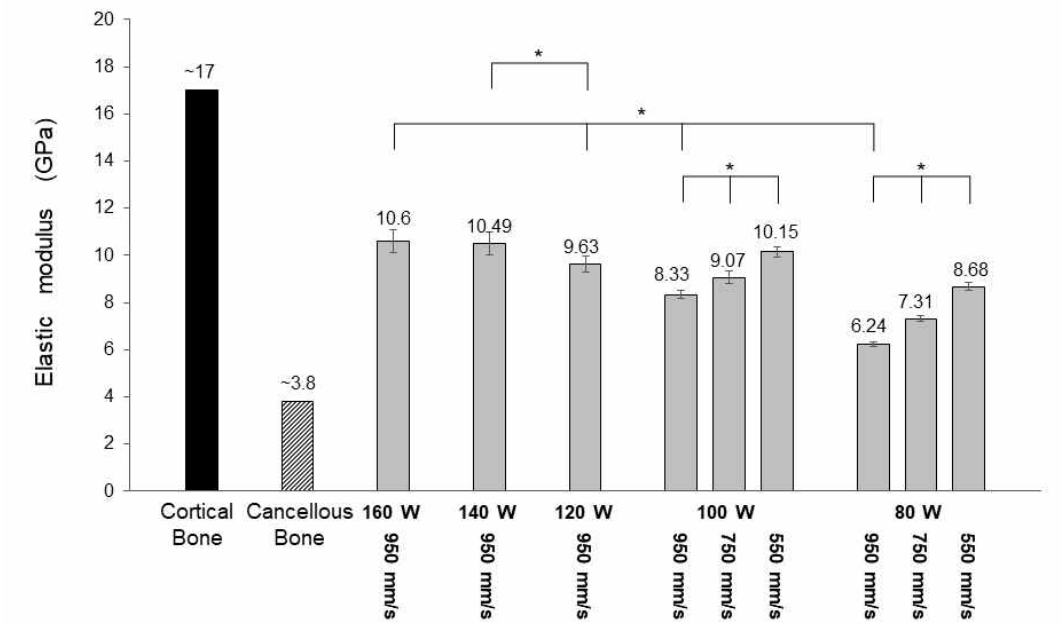

Figure 22. Elastic modulus of the specimens produced under various parameter settings (information for actual bone is sourced from the literature [72-75]). The results are presented as mean ± standard deviation with asterisks denoting $P < 0.05$.

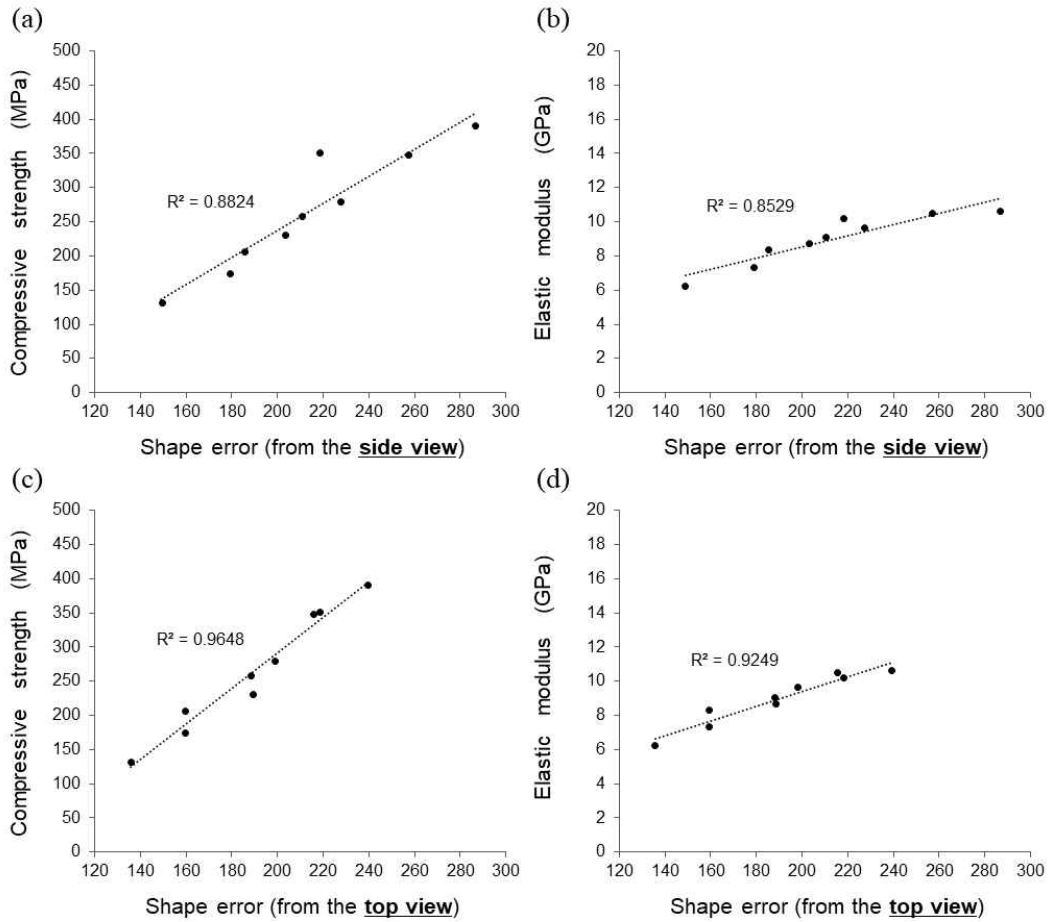

Figure 23. Scatter plots displaying the mechanical properties in relation to (a-b) side-view shape error and (c-d) top-view shape error. The R^2 value represents the coefficient of determination.

Table 4. Changes of shape errors and mechanical properties in response to decreasing laser power (160-80 W) at a constant scan speed of 950 mm/s.

Laser power (W)	Scan speed (mm/s)	Side-viewed shape error (μm)	Top-viewed shape error (μm)	Compressive Strength (MPa)	Elastic modulus (GPa)
160	950	▽0%	▽0%	▽0%	▽0%
140	950	▽11%	▽10%	▽11%	▽1%
120	950	▽21%	▽17%	▽28%	▽9%
100	950	▽36%	▽33%	▽47%	▽21%
80	950	▽48%	▽43%	▽66%	▽41%

Table 5. Changes of shape errors and mechanical properties in response to increasing scan speed (550-950 mm/s) at a constant laser power of 100 W.

Laser power (W)	Scan speed (mm/s)	Side-viewed shape error (μm)	Top-viewed shape error (μm)	Compressive Strength (MPa)	Elastic modulus (GPa)
100	550	▽0%	▽0%	▽0%	▽0%
100	750	▽3%	▽9%	▽26%	▽11%
100	950	▽15%	▽23%	▽41%	▽18%

Table 6. Changes of shape errors and mechanical properties in response to increasing scan speed (550-950 mm/s) at a constant laser power of 80 W.

Laser power (W)	Scan speed (mm/s)	Side-viewed shape error (μm)	Top-viewed shape error (μm)	Compressive Strength (MPa)	Elastic modulus (GPa)
80	550	▽0%	▽0%	▽0%	▽0%
80	750	▽12%	▽16%	▽25%	▽16%
80	950	▽27%	▽28%	▽43%	▽28%

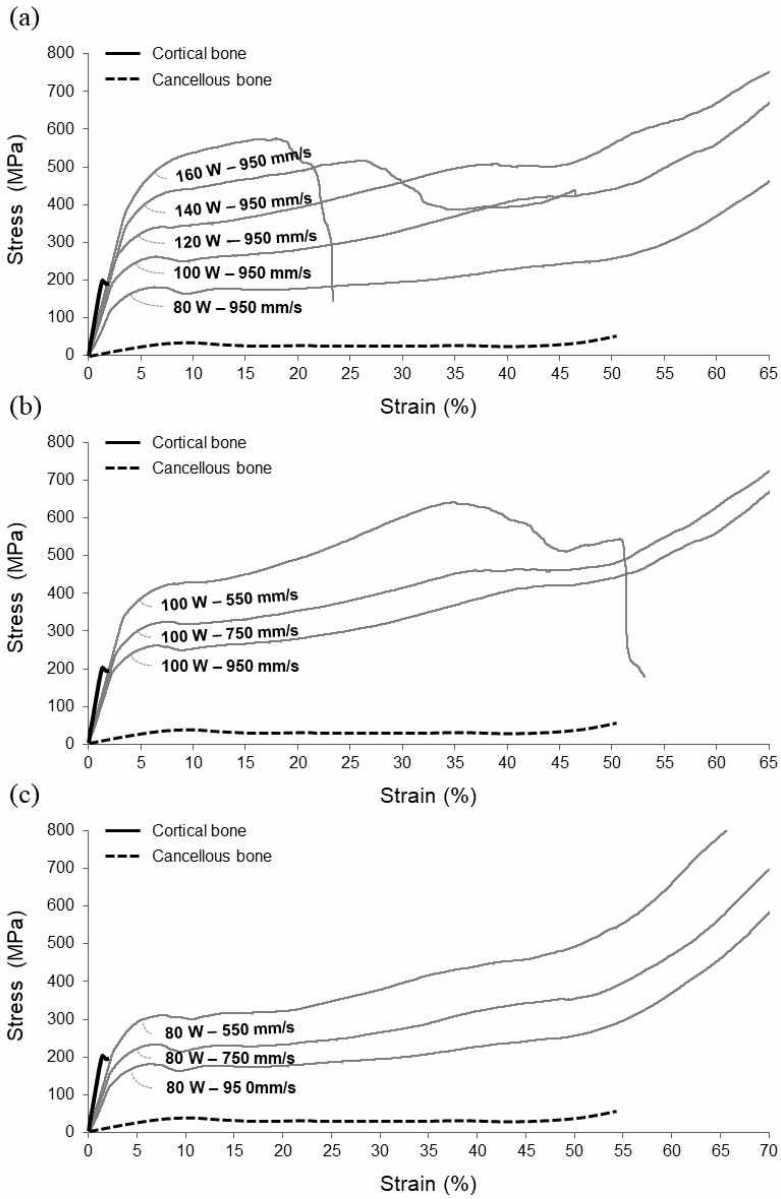

Figure 24. Stress-strain curves according to (a) various laser powers at a constant scan speed of 950 mm/s, (b) various scan speeds at a constant laser power of 100 W, and (c) various scan speeds at a constant laser power of 80 W (information for actual bone is sourced from the literature [82]).

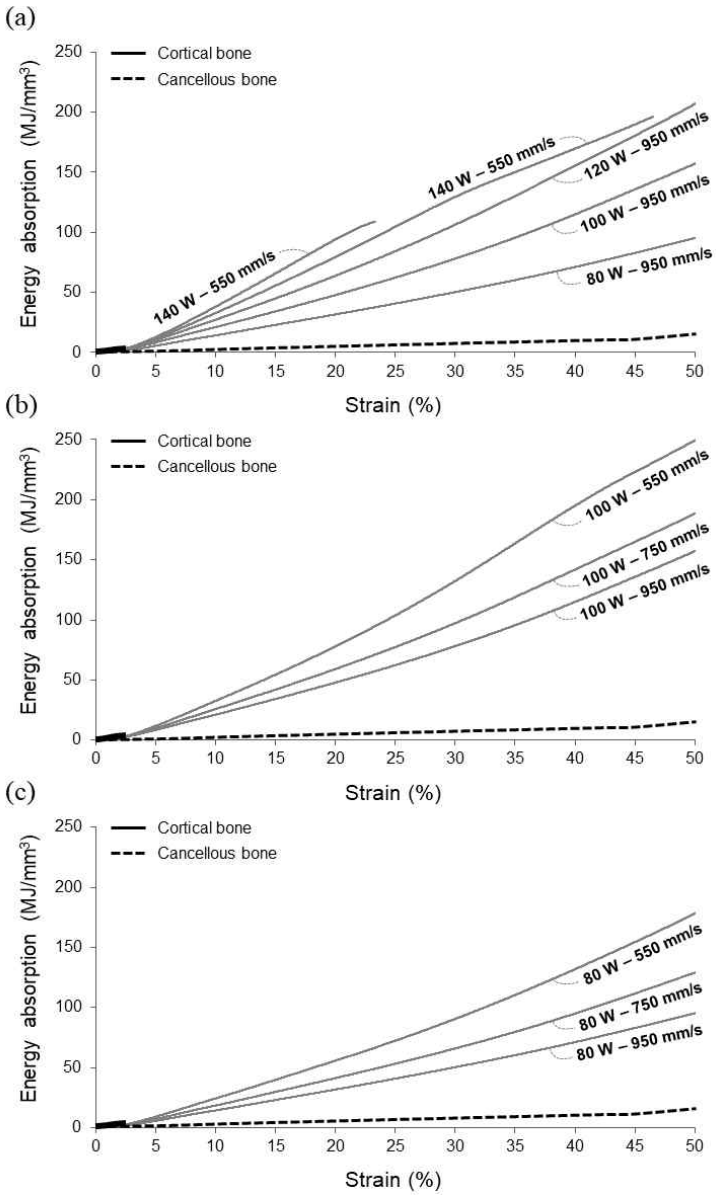

Figure 25. Energy absorption-strain curves according to (a) various laser powers at a constant scan speed of 950 mm/s, (b) various scan speeds at a constant laser power of 100 W, and (c) various scan speeds at a constant laser power of 80 W (information for actual bone is sourced from the literature [82]).

3. Enhancement of osseointegration

Figure 26-28 displays the in-vivo test results from this study. In two-week implantations, there was no significant difference between the groups in bone-to-implant contact (BIC): 83.53% ± 9.97%, 80.03% ± 13.84%, and 80.38% ± 11.45% in bone template porous structure, irregular porous structure, and regular lattice porous structure, respectively. However, in six-week implantations, the bone-templated and irregular porous structures showed significantly enhanced BIC levels (88.14% ± 9.2% and 94.25% ± 2.56%, respectively) compared to the regular lattice one (79.2% ± 11.41%) (see Figure 26). Regardless of the implantation periods, all groups showed excellent absent nearly 5% of absent areas without statistical significances (see Figure 26).

For a short period of two weeks, new bone with new blood vessels appeared to be equally generated throughout the implantation region. However, for an extended period of six weeks, the bone area within a 500 μm distance (encompassing only the porous structure region) was significantly greater than that within a 2000 μm distance (encompassing the outside of the porous structure as well) (see Figure 27). Takaoka Y et al. discovered that up to four weeks following the implantation of a porous scaffold are critical for establishing blood flow channels and activating subsequent cell migration [83]. In fact, in their in-vivo test results, the bone formation inside the structure increased rapidly from the second week of implantation. Conversely, the bone formation outside the structure either ceased to grow or decreased after the second week. Our findings align with this previous suggestion.

Interestingly, in an extended period of six-week implantations, the bone-templated and irregular porous structures tended to retain more bone area than the regular lattice porous structure. This tendency was statistically significant in 2000 μm observation.

Specifically, those of the former complex designs maintained the bone area at about 25-35% throughout the periods. In contrast, the latter simple design greatly decreased from about 30% (week 2) to about 10% (week 6) (see Figures 27 and 28). This result may further underline that the porous structure with irregular pore sizes can be more advantageous for osseointegration than those with a fixed size, as reported in a few other available references.

However, for a fair comparative study, we tuned the porosities of all porous structures to approximately 63% based on the bone template as a standard of bio-inspired modeling. This decision was made because while it was easy to measure porosity, defining pore size in the bone template was challenging due to its oriented geometry. Consequently, we achieved almost the same porosities. However, the average pore sizes differed between the irregular porous structure and the regular lattice porous structure (600 vs 400 μm) – the bone template likely had a similar average to the former. As mentioned in the backgrounds chapter, 600 μm rather than 400 μm is considered ideal for osseointegration, which may have been an additional cause of the above difference.

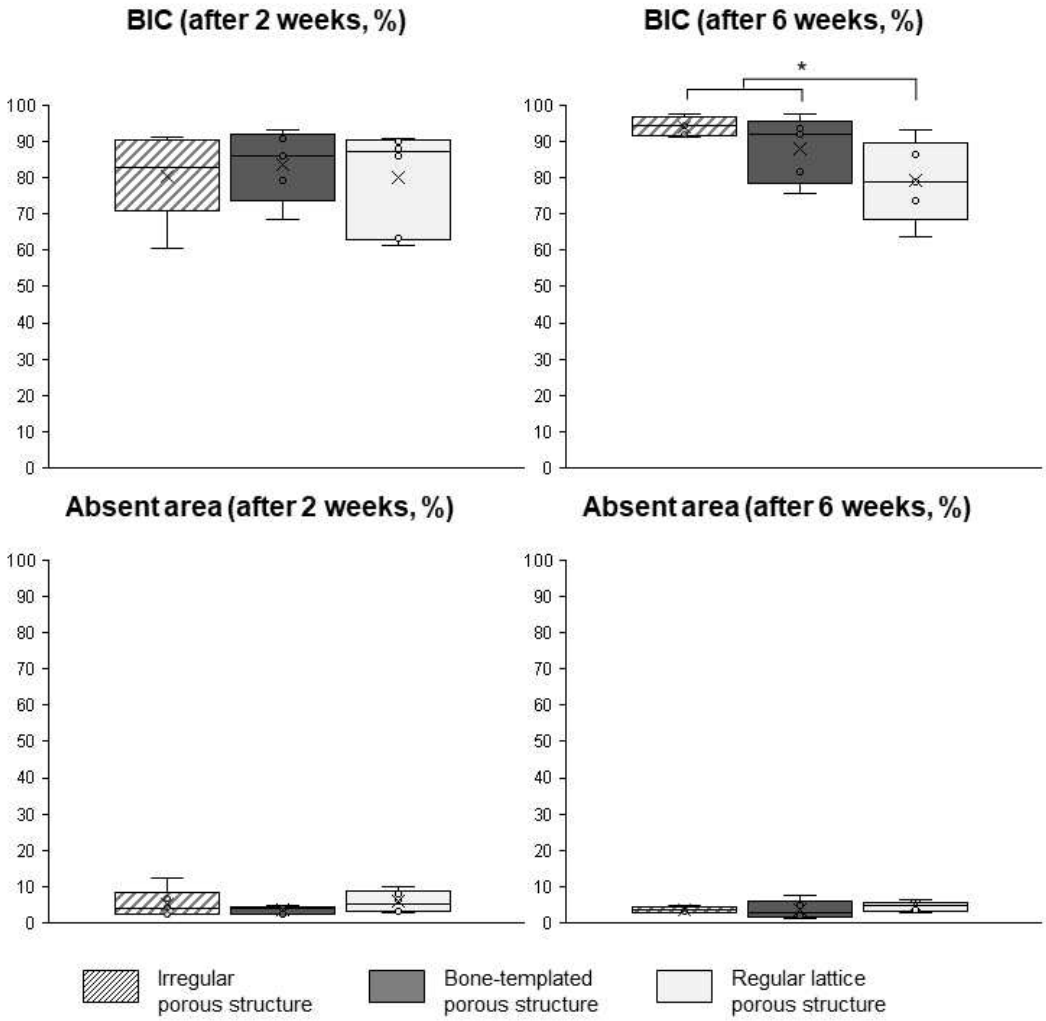

Figure 26. Bone histomorphometry results: bone-to-implant contact (BIC) and absent area according to different implantation periods and porous structure designs. Asterisks denotes $P < 0.05$.

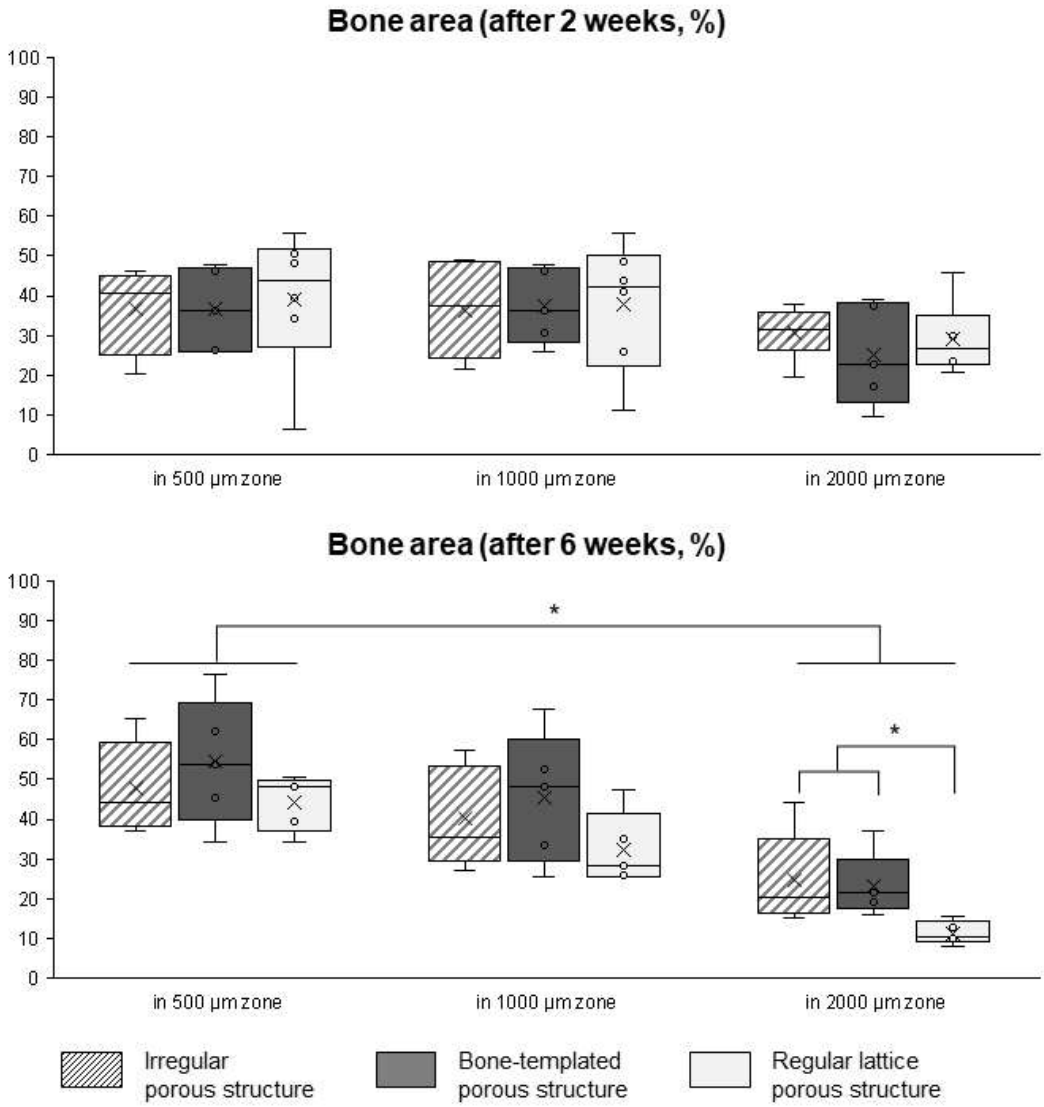

Figure 27. Bone histomorphometry results: bone area according to different implantation periods and porous structure designs. Asterisks denotes $P < 0.05$.

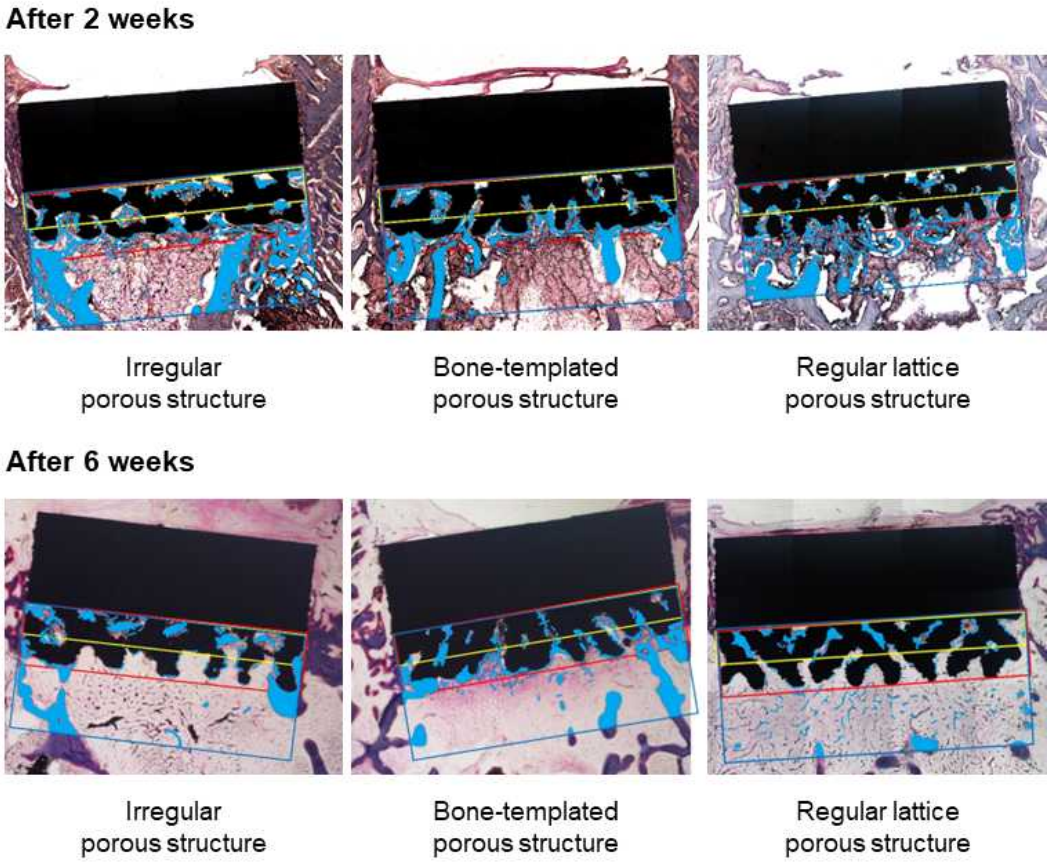

Figure 28. Representative histological images according to different implantation periods and porous structure designs. Blue pixels indicate bone area.

V. CONCLUSION

The current study included developing a new bone-mimetic design for porous structures based on Voronoi tessellation. Initially, we carried out optimization work on the manufacturing process, highlighting the critical influence of SLM laser parameters in achieving fine quality. The key findings are outlined below.

- Upregulation of the laser power or downregulation of the scan speed drove the pores narrower than the original design. Notably, stronger laser powers had a more dominant impact on the shape of the pores than slower scan speeds.
- The pore shape error was consistently greater in the side view observation than in the top. Furthermore, more substantial laser power intensified this discrepancy, likely due to additional errors at the overhang struts.
- There was a clear relationship between the shape error and mechanical properties of the porous structure. A rise in shape error led to increased compressive strength and elastic modulus.
- Using the weakest laser power (80 W) and the fastest scan speed (950 mm/s) led to the most significant reduction in pore shape error. In particular, although the mechanical properties diminished during the effort to minimize the shape error, they remained at suitable levels for clinical use.

The results obtained contribute to enhancing the understanding of the fine manufacturing strategies for recent porous orthopedic implants. In contrast to conventional solid products that typically prioritize the maximization of mechanical

properties, porous products may require a different parameter tunning that intends to maintain pore design. However, our study was limited to modifying only two laser parameters and addressing a few inputs. Additionally, the biological performances of the fabricated porous structures have yet to be compared. Thus, future research must arrive at more comprehensive and reliable conclusions by incorporating other variables, expanding the sample size, and conducting parametric in-vivo tests.

Next, we supported the promising osseointegration potential of the developed porous structure through an animal experiment. The following summarizes the key findings.

- The novel irregular porous structure exhibited compatible biological performance with the bone-templated porous structure.
- During the mid-term implantation period, the above actual bone and highly-bone-mimetic porous structures consistently maintained bone formation regardless of the observation region, while the regular lattice porous structure showed a significant decrease in bone area within a 2000 μm distance.

The obtained results contribute to resolving the scarcity of in-vivo references related to the importance of adopting the actual bone irregularity in the designs of porous structures. However, as discussed, it is difficult to rule out the possibility that the different pore size averages with the controlled porosities may have additionally influenced the results. In other words, to achieve a clearer conclusion, future studies should be conducted with the different porosities with the controlled

pore size averages. Also, long-term implantations for more than six weeks will be necessary to further investigate the difference in bone formation retention.

Appendices

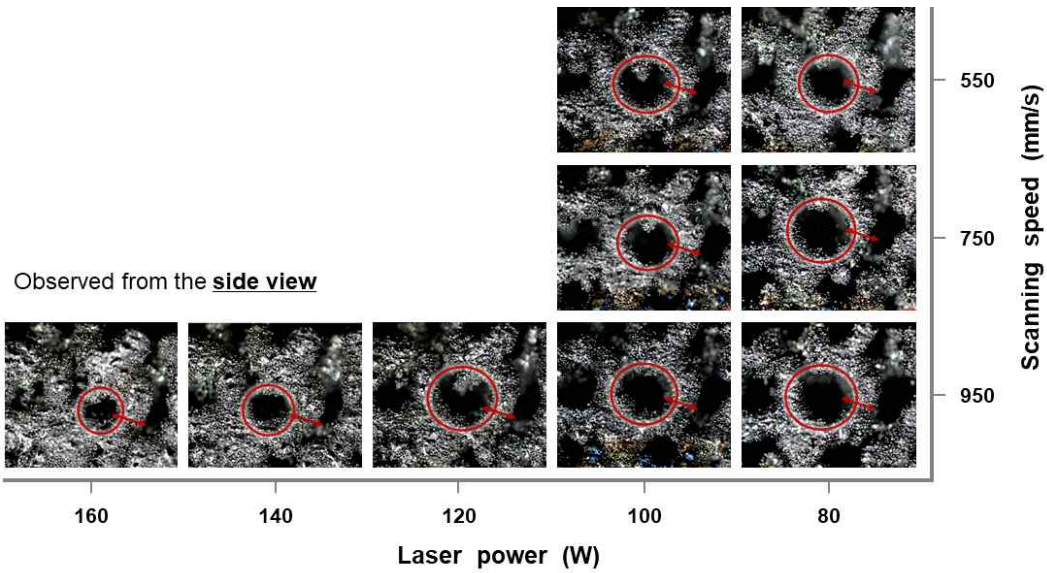

Figure A1. Side-viewed pore shape changes observed by optical microscopy according to different parameter sets.

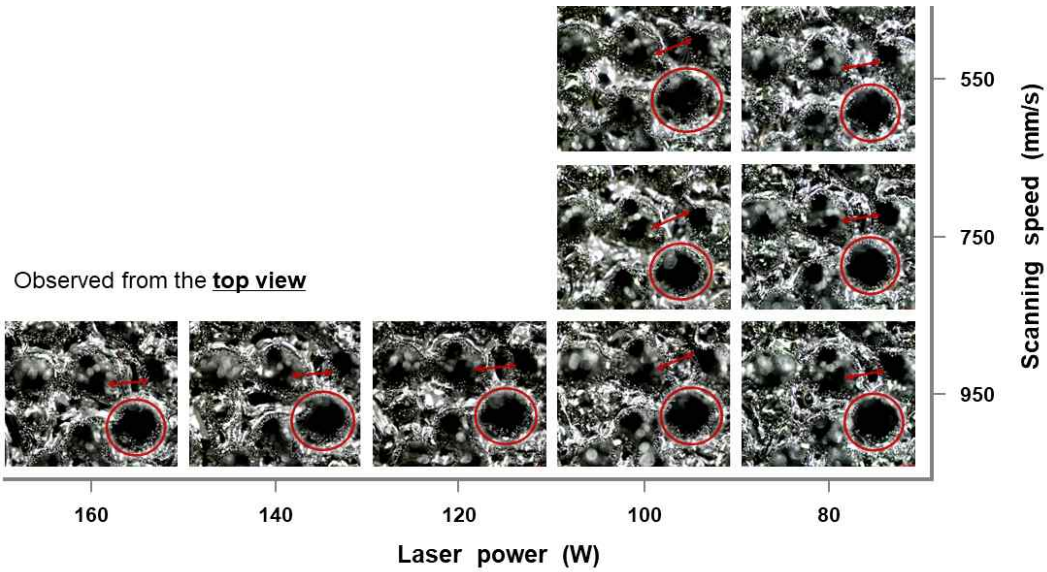

Figure A2. Top-viewed pore shape changes observed by optical microscopy according to different parameter sets.

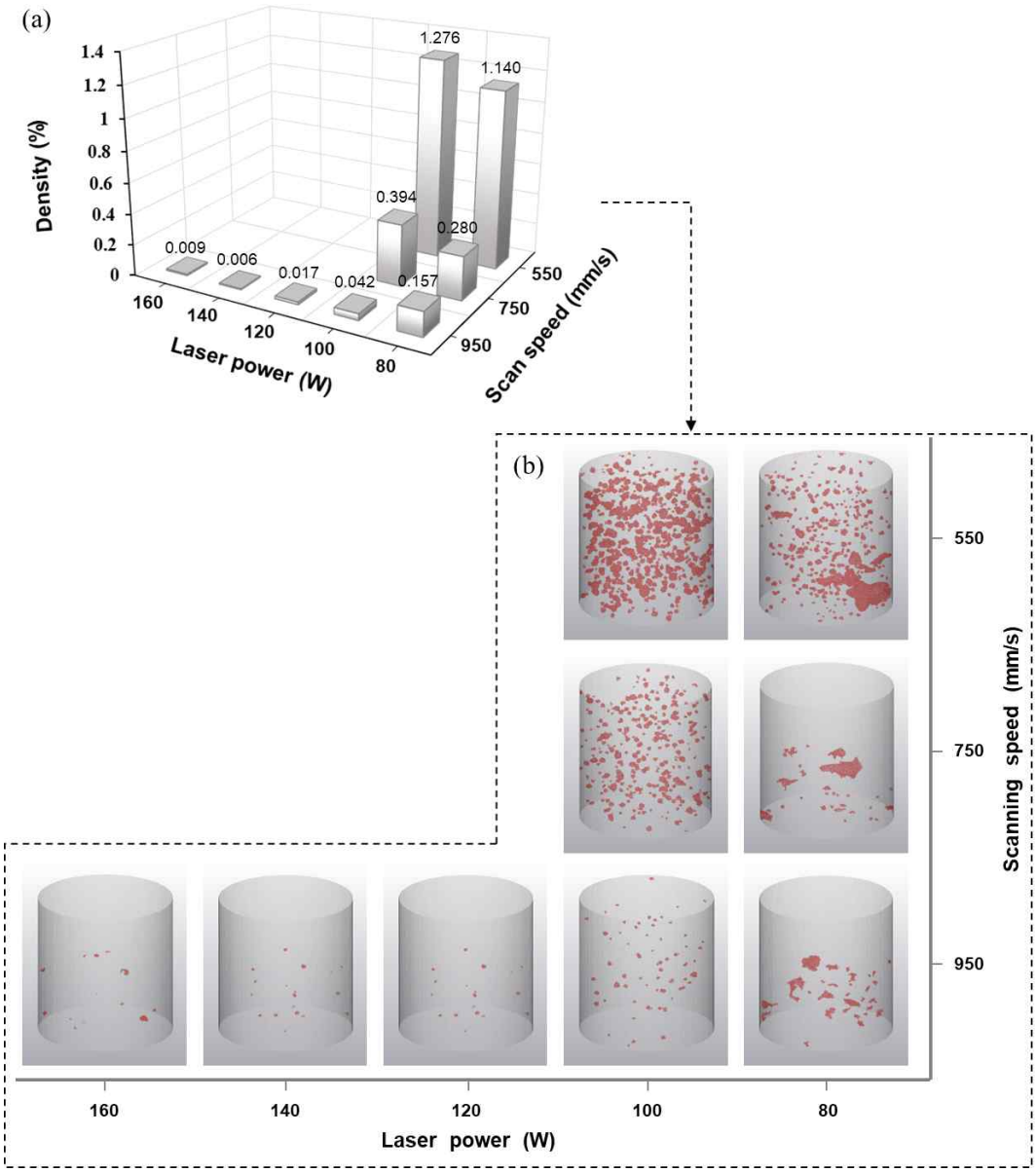

Figure A3. (a) Densities of bulk solid specimens under different parameter sets; (b) Visualization of the internal defect changes using the 3D-reconstructed models

References

1. Walsh WR, Pelletier MH, Bertollo N, Lovric V, Wang T, Morberg P, WCH Parr, Bergadano D (2020) Bone ongrowth and mechanical fixation of implants in cortical and cancellous bone. J Orthop Surg Res 15(1):177.

2. Harwin SF, Elmallah RK, Jauregui JJ, Cherian JJ, Mont MA (2015) Outcomes of a Newer-Generation Cementless Total Knee Arthroplasty Design. Orthopedics 38(10):620-624.

3. Harwin SF, Patel NK, Chughtai M, Khlopas A, Ramkumar PN, Roche M, Mont MA (2017) Outcomes of newer generation cementless total knee arthroplasty: Beaded periapatite-coated vs highly porous titanium-coated implants. J Arthroplasty 32(7):2156–2160.

4. Miller AJ, Stimac JD, Smith LS, Feher AW, Yakkanti MR, Malkani AL (2018) Results of cemented vs cementless primary total knee arthroplasty using the same implant design. J Arthroplasty 33(4):1089-1093.

5. Laupacis A, Bourne R, Rorabeck C, Feeny D, Tugwell P, Wong C (2002) Comparison of total hip arthroplasty performed with and without cement: A randomized trial. J Bone Joint Surg Am 84(10):1823-1828.

6. Albrektsson T, Johansson C (2001) Osteoinduction, osteoconduction and osseointegration. Eur Spine J 10:S96-S101.

7. MacBarb RF, Lindsey DP, Bahney CS, Woods SA, Wolfe ML, Yerby SA (2017) Fortifying the bone-implant interface part 1: an in vitro evaluation of 3D-printed and TPS porous surfaces. Int J Spine Surg 11(3):15.

8. Bandyopadhyay A, Mitra I, Avila JD, Upadhyayula M, Bose S (2023) Porous metal implants: processing, properties, and challenges. Int J Extrem Manuf

5:032014.

9. Shin T, Park SJ, Kang KS, Kim JS, Kim Y, Lim Y, Lim D (2017) A laser-aided direct metal tooling technology for artificial joint surface coating. Int J Precis Eng Manuf 18:233–238.

10. Davey JR, Harris WH (1988) Loosening of cobalt chrome beads from a porous-coated acetabular component. A report of ten cases. Clin Orthop Relat Res 231:97-102.

11. Wu Y, Liu J, Kang L, Tian J, Zhang X, Hu J, Huang Y, Liu F, Wang H, Wu Z (2023) An overview of 3D printed metal implants in orthopedic applications: Present and future perspectives. Heliyon 9(7): e17718.

12. Kim J, Wakai A, Moridia A (2020) Materials and manufacturing renaissance: additive manufacturing of high-entropy alloys. J Mater Res 35(15):1-21.

13. Weißmann V, Drescher P, Bader R, Seitz H, Hansmann H, Laufer L (2017) Comparison of single Ti6Al4V struts made using selective laser melting and electron beam melting subject to part orientation. Metals 7(3): 91.

14. Depboylu FN, Yasa E, Poyraz Ö, Minguella-Canela J, Korkusuz F, De los Santos Lopez MA (2022) Titanium based bone implants production using laser powder bed fusion technology. J Mater Res Tech 17:1408-1426.

15. Joshua RJN, Raj SA, Sultan MTH, Łukaszewicz A, Józwik J, Oksiuta Z, Dziedzic K, Tofil A, Shahar FS (2024) Powder bed fusion 3D printing in precision manufacturing for biomedical applications: A comprehensive review. Materials 17(3):769.

16. Nouri A, Hodgson PD, Wen C (2010) Biomimetic porous titanium scaffolds for orthopedic and dental applications. In: Amitava M (ed) Biomimetics learning from nature. Intech, Rijeka, pp.415-450.

17. Pałka K and Pokrowiecki R (2018) Porous titanium implants: A Review. Adv Eng Mater 20(5):1700648.

18. Talukdar RG , Dhara S, Gupta S (2024) Bone ingrowth in randomly distributed porous interbody cage during lumbar spinal fusion. Med Eng Phys 133: 104248.

19. Cheng A, Humayun A, Cohen DJ, Boyan BD, Schwartz Z (2014) Additively manufactured 3D porous Ti-6Al-4V constructs mimic trabecular bone structure and regulate osteoblast proliferation, differentiation and local factor production in a porosity and surface roughness dependent manner. Biofabrication 6(4):045007.

20. Podshivalov L, Gomes CM, Zocca A, Guenster J, Bar-Yoseph P, Fischer A (2013) Design, analysis and additive manufacturing of porous structures for biocompatible micro-scale scaffold. Procedia CIRP 5:247-252.

21. Wang X, Xu S, Zhou S, Xu W, Leary M, Choong P, Qian M, Brandt M, Xie YM (2016) Topological design and additive manufacturing of porous metals for bone scaffolds and orthopaedic implants: A review. Biomaterials 83:127-141.

22. Lv Y, Wang B, Liu G, Tang Y, Lu E, Xie K, Lan C, Liu J, Qin Z, Wang L (2021) Metal material, properties and design methods of porous biomedical scaffolds for additive manufacturing: A review. Front Bioeng Biotech 9:641130.

23. Taniguchi N, Fujibayashi S, Takemoto M, Sasaki K, Otsuki B, Nakamura T, Matsushita T, Kokubo T, Matsuda S (2016) Effect of pore size on bone ingrowth into porous titanium implants fabricated by additive manufacturing: An in vivo experiment. Mater Sci Eng C Mater Biol Appl 59:690-701.

24. Guo Y, Chen C, Wang QB, Lu M, Cao YK, Pan YM, Tan LM (2022)

Effect of porosity on mechanical properties of porous tantalum scaffolds produced by electron beam powder bed fusion. Trans Nonferrous Met Soc China 32:2922-2934.

25. Chao L, He Y, Gu J, Xie D, Yang Y, Shen L, Wu G, Wang L, Tian Z, Liang H (2023) Design of porous structure based on the Voronoi diagram and stress line for better stress shielding relief and permeability. J Mater Res Tech 25:1719-1734.

26. Fantini M, Curto M, Crescenzio FD (2016) A method to design biomimetic scaffolds for bone tissue engineering based on Voronoi lattices. Virtual Phys Prototyp 11(2):1-14.

27. Dua Y, Liang H, Xie D, Mao N, Zhao J, Tian Z, Wang C, Shen L (2020) Design and statistical analysis of irregular porous scaffolds for orthopedic reconstruction based on voronoi tessellation and fabricated via selective laser melting (SLM). Mater Chem Phys 239:121968.

28. Gómez S, Vlad MD, López J, Fernández E (2016) Design and properties of 3D scaffolds for bone tissue engineering. Acta Biomaterialia 42(15):341-350.

29. Wang G,Shen L, Zhao J, Liang H, Xie D, Tian Z, Wang C (2018) Design and compressive behavior of controllable irregular porous scaffolds: based on voronoi-tessellation and for additive manufacturing. ACS Biomater Sci Eng 4(2):719-727.

30. Zhao H, Han Y,Pan C, Yang D, Wang H, Wang T, Zeng X, Su P (2021) Design and mechanical properties verification of gradient voronoi scaffold for bone tissue engineering. Micromachines 12(6):664.

31. Chen W, Dai N, Wang J, Liu H, Li D, Liu L (2019) Personalized design of functional gradient bone tissue engineering scaffold. J Biomech Eng 141(11):111004.

32. Liang H, Yang Y, Xie D, Li L, Mao N, Wang C, Tian Z, Jiang Q, Shen L (2019) Trabecular-like Ti-6Al-4V scaffolds for orthopedic: fabrication by selective laser melting and in vitro biocompatibility. J Mater Sci Technol 35(7):1284-1297.

33. Gradl P, Tinker DC, Park A, Mireles OR, Garcia M, Wilkerson R, Mckinne C (2022) Robust metal additive manufacturing process selection and development for aerospace components. J Mater Eng Perf Perform 31:6013-6044.

34. Javidrad HR, Javidrad F (2023) Review of state-of-the-art research on the design and manufacturing of support structures for powder-bed fusion additive manufacturing. Prog Addit Manuf 8:1517–1542.

35. Ahmadi M, Bozorgnia Tabary SAA, Rahmatabadi D, Ebrahimi MS, Abrinia K, Hashemi R (2022) Review of selective laser melting of magnesium alloys: advantages, microstructure and mechanical characterizations, defects, challenges, and applications. J Mater Res Tech 19:1537-1562.

36. Olakanmi EO, Cochrane RF, Dalgarno KW (2015) A review on selective laser sintering/melting (SLS/SLM) of aluminium alloy powders: Processing, microstructure, and properties. Prog Mater Sci 74:401-477.

37. Kaya G, Yıldız F, Korkmaz İ.H, Kaymaz İ, Yetim AF, Ergüder TO, Şen Ç (2023) Effects of process parameters on selective laser melting of Ti6Al4V-ELI alloy and parameter optimization via response surface method. Mater Sci Eng A 885:145581.

38. Ferro P, Meneghello R, Savio G, Berto F (2020) A modified volumetric energy density–based approach for porosity assessment in additive manufacturing process design. Int J Adv Manuf Tech 110:1911-1921.

39. Charles A, Ahmed E, Thijs L, Scholz SG (2020) Dimensional errors due to

overhanging features in laser powder bed fusion parts made of Ti-6Al-4V. Appl Sci 10(7):2406.

40. Pal S, Kokol V, Gubeljak N, Hadžistević M, Hudak R, Drstvenšek I (2019) Dimensional errors in selective laser melting products related to different orientations and processing parameters. Mater Tech 53(4):551-558.

41. Loh QL, Choong C (2013) Three-dimensional scaffolds for tissue engineering applications: Role of porosity and pore size. Tissue Eng Part B Rev 19(6):485-502.

42. Mohammadi H, Sepantafar M, Muhamad N, Sulong AB (2021) How does scaffold porosity conduct bone tissue regeneration? Adv Eng Mater 23(10):2100463.

43. Frosch KH, Barvencik F, Lohmann CH, Viereck V, Siggelkow H, Breme J, Dresing K, Stürmer KM (2002) Migration, matrix production and lamellar bone formation of human osteoblast-like cells in porous titanium implants. Cells Tissues Organs 170(4):214–227.

44. Fukuda A, Takemoto M, Saito T, Fujibayashi S, Neo M, Pattanayak DK, Matsushita T, Sasaki K, Nishida N, Kokubo T, Nakamura T (2011) Osteoinduction of porous Ti implants with a channel structure fabricated by selective laser melting. Acta Biomater 7(5):2327-2336.

45. Ran Q, Yang W, Hu Y, Shen X, Yu Y, Xiang Y, Cai K (2018) Osteogenesis of 3D printed porous Ti6Al4V implants with different pore sizes, Journal of the Mechanical. J Mech Behav Biomed Mater 84:1-11.

46. Ouyang P, , Dong H, He X, Cai X, Wang Y, Li J, Li H, Jin Z (2019) Hydromechanical mechanism behind the effect of pore size of porous titanium scaffolds on osteoblast response and bone ingrowth. Meter Des 183:108151.

47. Van Bael S, Kerckhofs G, Moesen M, Pyka G, Schrooten J, Kruth JP (2011) Micro-CT-based improvement of geometrical and mechanical controllability of selective laser melted Ti6Al4V porous structures. Mater Sci Eng A 525(24):7423-7431.

48. Shi X, Sun Y, Wang P, Ma Z, Liu H, Ning H (2021) Compression properties and optimization design of SLM Ti6Al4V square pore tissue engineering scaffolds. Proc Inst Mech Eng H 235(11):1265-1273.

49. Gao H, Jin X, Yang J, Zhang D, Zhang S, Zhang F, Chen H (2021) Porous structure and compressive failure mechanism of additively manufactured cubic-lattice tantalum scaffolds. Mater Today Adv 12:100183.

50. Karageorgiou V, Kaplan D (2005) Porosity of 3D biomaterial scaffolds and osteogenesis. Biomaterials 26(27):5474-5491.

51. Van Bael S, Chai YC, Truscello S, Moesen M, Kerckhofs G, Oosterwyck HV, Kruth JP, Schrooten J (2012) The effect of pore geometry on the in vitro biological behavior of human periosteum-derived cells seeded on selective laser-melted Ti6Al4V bone scaffolds. Acta Biomater 8(7):2824-2834.

52. Depboylu FN, Yasa E, Poyraz Ö, Korkusuz Feza, Popa AA (2024) Choosing between commercially pure titanium and Ti-6Al-4V gyroid structures for orthopedic applications: An analysis through Timoshenko beam theory, the Gibson-Ashby model and experimental methods. Mater Today Commun 39:109256.

53. Abd-Elaziem W, Darwish MA, Hamadad A, Daoush, WM (2024) Titanium-Based alloys and composites for orthopedic implants applications: A comprehensive review. Mater Des 241:112850.

54. Quinn J, McFadden R, Chan CW, Carson L (2020) Titanium for orthopedic applications: an overview of surface modification to improve biocompatibility

and prevent bacterial biofilm formation. iScience 23(11):101745.

55. Gupta SK, Shahidsha N, Bahl S, Kedaria D, Singamneni S, Yarlagadda PKDV, Suwas S, Chatterjee K (2021) Enhanced biomechanical performance of additively manufactured Ti-6Al-4V bone plates. J Mech Behav Biomed Mater 119:104552.

56. Raval J, Kazi A, Randolph O, Guo X, Zvanut R, Lee C, Tai B (2023) Machinability comparison of additively manufactured and traditionally wrought Ti-6Al-4V alloys using single-point cutting. J Manuf Proc 94:539-549.

57. Ryan G, Pandit A, Apatsidis DP (2006) Fabrication methods of porous metals for use in orthopedic applications. Biomaterials 27(13):2651-2670.

58. Lv Y, Wang B, Liu G, Tang Y, Liu J, Wei G, Wang L (2022) Design of bone-like continuous gradient porous scaffold based on triply periodic minimal surfaces. J Mater Res Tech 21:3650-3665.

59. Guo Y, Chen C, Wang QB, Liu M, Cao YK, Pan YM, Tan LM (2022) Effect of porosity on mechanical properties of porous tantalum scaffolds produced by electron beam powder bed fusion. Trans Nonferrous Met Soc China 32:2922-2934.

60. Yang J, Gao H, Zhang D, Jin X, Zhang F, Zhang S, Chen H, Li X (2021) Static Compressive Behavior and Material Failure Mechanism of Trabecular Tantalum Scaffolds Fabricated by Laser Powder Bed Fusion-based Additive Manufacturing. Int J Bioprint 8(1):438.

61. Salem H, Carter LN, Attallah MM, Salem HG (2019) Influence of processing parameters on internal porosity and types of defects formed in Ti6Al4V lattice structure fabricated by selective laser melting. Mater Sci Eng A 767(8):138387.

62. Liu J, Liu B, Min S, Yin B, Peng B, Yu Z, Wang C, Ma X, Wen P, Tian Y, Zheng Y (2022) Biodegradable magnesium alloy WE43 porous scaffolds fabricated by laser powder bed fusion for orthopedic applications: Process optimization, in vitro and in vivo investigation. Bioact Mater 16:301-319.

63. Ryu DJ, Ban HY, Jung EY, Sonn CH, Hong DH, Ahmad S, Gweon B, Lim D, Wang JH (2020) Osteo-compatibility of 3d titanium porous coating applied by direct energy deposition (DED) for a cementless total knee arthroplasty implant: in vitro and in vivo study. J Clin Med 9(2):478.

64. Thomas D (2009). The development of design rules for selective laser melting. Dissertation, University of Wales.

65. Wu F, Sun Z, Chen W, Liang Z (2021) The effects of overhang forming direction on thermal behaviors during additive manufacturing Ti-6Al-4V Alloy. Materials 14(13):3749.

66. Ghaoui S, Ledoux Y, Vignat F, Museau M, Vo TH, Villeneuve F, Ballu A (2020) Analysis of geometrical defects in overhang fabrications in electron beam melting based on thermomechanical simulations and experimental validations. Addit Manuf 36(5):101557.

67. Jiang D, Ning F (2022) Anisotropic deformation of 316L stainless steel overhang structures built by material extrusion based additive manufacturing. Addit Manuf 50:102545.

68. Arputharaj JD, Nafisi S, Ghomashchi R (2024) Printability and geometric capability of L-PBF in manufacturing thin circular cross-sections. J Manuf Proc 129:319-340.

69. Yang L, Ferrucci M, Mertens R, Dewulf W, Yan C, Shi Y, Yang S (2020) An investigation into the effect of gradients on the manufacturing fidelity of triply periodic minimal surface structures with graded density fabricated by

selective laser melting.

70. Bertocco A, Iannitti G, Caraviello A, Esposito L (2022) Lattice structures in stainless steel 17-4PH manufactured via selective laser melting (SLM) process: dimensional accuracy, satellites formation, compressive response and printing parameters optimization. Int J Adv Manuf Tech 120:4935–4949.

71. Yu X, Wu J, Zhong K, Wang Z, Zhao Y, Zhao J (2024) Mechanical predictive modeling of stereolithographic additive manufactured alumina microlattices. Int J Mech Sci 262:108752.

72. Öhman C, Baleani M, Pani C, Taddei F, Alberghini M, Viceconti M, Manfrini M (2011) Compressive behaviour of child and adult cortical bone. Bone 49(4):769-776.

73. Gerhardt LC, Boccaccini AR (2010) Bioactive glass and glass-ceramic scaffolds for bone tissue engineering. materials 3(7): 3867-3910.

74. Heary RF, Parvathreddy N, Sampath S, Agarwal N (2017) Elastic modulus in the selection of interbody implants. J Spine Sur 3(2):163-167.

75. Hong J, Cha H, Park Y, Lee S, Khang G, Kim Y (2007). Elastic moduli and poisson's ratios of microscopic human femoral trabeculae. In: Jarm T, Kramar P, Zupanic A (eds) 11th Mediterranean Conference on Medical and Biomedical Engineering and Computing 2007, IFMBE, vol 16. Springer, Berlin, pp 274–277.

76. Luo Y, Wang, M, Tu J. Jiang Y, Jiao S (2021) Reduction of residual stress in porous Ti6Al4V by in situ double scanning during laser additive manufacturing. Int J Miner Metall Mater 28(3):1844–1853.

77. Lin C, Kang J (2021) Mechanical properties of compact bone defined by the stress-strain curve measured using uniaxial tensile test: a concise review and

practical guide. Materials 14(15):4224.

78. Khoa ND, Bohara RP, Ghazlan A, Thai T, Ngo T (2024) Novel hierarchical bioinspired cellular structures with enhanced energy absorption under uniaxial compression. J Aerosp Sci Tech 147:108995.

79. Sheng X, Guo A, Guo S, Sui S, Yang W, Tang R, Li X, Qu P, Wang M, Lin X (2024) Laser powder bed fusion for the fabrication of triply periodic minimal surface lattice structures: Synergistic macroscopic and microscopic optimization. J Manuf Proc 119(15):179-192.

80. Ziaie B, Velay X, Saleem W (2024) Advanced porous hip implants: a comprehensive review. Heliyon e37818.

81. Morita M, Sasada T (1996) Fatigue fracture mechanism of cancellous bone. In: Hayashi K, Kamiya A, Ono K (eds) Biomechanics. Springer, Tokyo, pp.141-167.

82. Mercer C, He MY, Wang R, Evans AG (2006) Mechanisms governing the inelastic deformation of cortical bone and application to trabecular bone. Acta Biomater 2(1):59-68.

83. Takaoka Y, Fujibayashi a, Onoe H, Goto K, Otsuki B, Kawai T, Okuzu Y, Shimizu T, Ikeda N, Orita K, Honda S, Ikezaki T, Yabutsuka T, Matsuda S (2024) Bone ingrowth into a porous structure is achieved by preceding fibrogenesis and vascularization. Acta Biomaterialia 177: 243-252.

국문요약

뼈 모방 비규칙 설계를 가진 3D 프린팅 다공성 구조의 골유합 효과에 대한 연구

반훈영

생체공학협동과정
연세대학교 대학원

다공성구조는 골조직과 임플란트 사이에서 골유합 즉, 강력한 생물학적 고정을 유도하며, 전통적인 수술과정에서 사용되는 골시멘트를 대체하는 역할을 수행한다. 한편, 3D 프린팅 기술은 정형외과 분야에서 강력한 임플란트 제조 플랫폼으로 자리잡고 있는데, 그 중 선택적 레이저 용융 방식 (Selective Laser Melting, SLM)은 특히나 뛰어난 해상도를 자랑한다. 당연하게도, 복잡한 뼈 모사 다공성구조를 임플란트 설계에 포함시키고 이를 SLM을 통해 제조해내는 것이 주요 트렌드가 되어가고 있다.

최근 주목받고 있는 보로노이 테셀레이션 모델링 기법은 비규칙적 크기를 가지는 기공들을 생성시킴으로써 실제 뼈와 매우 유사한 다공성구조를 구현할 수 있게 한다. 다만, 임상에 광범위하게 적용되기에는 선행되어 확인될 부분들

이 존재하는데, 우선 그 생물학적 성능에 대한 비교검증 사례가 거의 없다. 또한 그러한 복잡한 다공성구조를 미세 제조함에 있어 그 품질을 보장하기 위한 공정 최적화 연구가 부족하다. 따라서, 본 연구는 이 두가지 잔존 과제들을 해소하는데 목적을 두고 진행되었다.

구체적으로, 보로노이 테셀레이션 모델링 기법을 기반으로 하는 자체 알고리즘을 개발하고, 비규칙적 다공성구조를 설계하였다. 그런 다음 우선, 그 SLM 제조 공정을 최적화하기 위하여 다양한 공정변수 세팅에서 시편을 제작하였다. 레이저파워는 80-160 W, 스캔스피드는 550-950 mm/s의 범위에서 각각 조작되었다. 이후 제작된 시편에 대하여 Micro-CT 촬영이 이루어졌으며, 획득된 단면 이미지에서 기공 형상 오차가 측정되었다. 또한, 기계적 물성은 압축 실험을 통해 확인되었다. 결과적으로, 기공은 레이저파워가 강할수록 스캔스피드가 느릴수록 협소해졌다 또한, 이러한 치수 부정확도가 커질수록 다공성구조의 기계적 물성도 강해지는 경향을 보였다 (양의 상관관계). 결과적으로 가장 약한 레이저파워(80 W) 및 가장 빠른 스캔스피드(950 mm/s)에서 기공의 크기 분포는 가장 설계와 가깝게 제작되었다. 이때, 최소화된 형상 오차(135-150 μm)에서 압축강도와 탄성계수는 각각 131.45 MPa와 6.24 GPa로 임상적 사용에 적합한 수준으로 유지되었다.

이어서, 그 골유합 증진 효과를 종래의 다공성구조(뼈 템플릿 다공성구조, 규칙적 격자 다공성구조)들과 비교하였다. 시편들은 SLM 장비와 Ti-6Al-4V 파우더를 사용하여 제작되었으며, 이어서 동물이식 및 조직학적 분석이 수행되었다. 결과적으로 비규칙적 다공성구조는 뼈 템플릿 다공성구조와 비슷한 생체 내 결과를 보였으며 특히, 6주간의 이식 기간 동안 뼈 형성을 유지하는 데 있어 규칙적 격자 다공성구조 대비 유의한 개선을 보였다.

종합적으로 도출된 결론은 다음과 같다. 1) 다공성구조 설계에 있어, 골유

합 개선을 위하여 실제 뼈의 비규칙성을 모사하는 것이 중요할 수 있다. 2) 그러한 복잡한 다공성구조의 제조에는 기공 형상 오차 최소화에 초점을 맞춘 별도의 SLM 공정조건이 필요할 수 있다. 끝으로, 본 연구결과는 다공성 요소(또는 영역)을 포함하는 최신 정형외과 임플란트의 설계 및 제조에 있어 필수적인 참조자료로 활용될 수 있을 것으로 기대된다.

핵심 되는 말: 비규칙적 다공성구조 · 골유합 · 3D 프린팅 · 선택적 레이저 용융 · 매개변수 연구 · 형상 오차 · 기계적 물성